Final work : Numerical investigation of the influence of geometric uncertainties on transonic compressor flows

Auteur : Palmese, Claudio
Promoteur(s) : Hillewaert, Koen
Faculté : Faculté des Sciences appliquées
Diplôme : Master en ingénieur civil en aérospatiale, à finalité spécialisée en "turbomachinery aeromechanics (THRUST)"
Année académique : 2022-2023
URI/URL : http://hdl.handle.net/2268.2/18223

TECHNISCHE
UNIVERSITÄT
DARMSTADT

University of Liège - School of Engineering and Computer Science

Numerical Investigation of the Influence of Geometric Uncertainties on Transonic Compressor Flows

Author

Claudio Palmese

Supervisors

Koen Hillewaert, Fabian Klausmann, Nicklas Kilian

Jury members

Vincent Terrapon, Koen Hillewaert, Fabian Klausmann

Master's thesis completed in order to obtain the degree of Master of Science in Civil and Aerospace Engineering with specialization in turbomachinery aeromechanics (THRUST)

Academic year 2022–2023

Abstract

Modern aeronautical engine development relies on a good computational prediction of flow quantities within the design process. Besides potential limitations in CFD related to flow modelling, a non-neglectable source of error can be related to geometric differences between the design and the final product, caused by wear and tear and manufacturing uncertainties. These variations do not simply impact the global performance of the machine, but may also give rise to flow phenomena that could change the stability limits of the machine or cause increased wear.
The Institute of Gas Turbines and Aerospace Propulsion at Technical University of Darmstadt conducted experiments in a 1.5-stage transonic axial compressor within the ARIAS project, funded by the Horizon2020 programme. In these measurements, a blade-to-blade variation in flow quantities could be observed at the rotor tip with Particle Image Velocimetry and unsteady pressure measurements. The aim of this work is hence to analyse the influence on the compressor flow of potential geometric uncertainties in the rotor blades by means of a parametrization of the original CAD geometry. By doing so, it becomes possible to set up an automated script that generates blades which differ from the standard in one or more aspects, according to real geometric variations. A feasible reference domain of the 1.5 stage transonic compressor is first created with the CAD model and analysed. Then, the rotor blade is parametrized and compared both in geometry and performance to the reference setup. The parametrized blade is then used as a base to generate sets of modified blades, which are each studied in single-passage simulations in order to compare the consequent flow variations. Finally, a full-annulus simulation is set up where only a single blade is modified in its stagger angle, with the objective of capturing blade-to-blade flow variations.
The flow seems to be highly sensitive to leading edge curl, with significant sensitivity to trailing edge curl and leading edge thickness, while limited change was recorded with the chosen amount of stagger angle change. When misstaggering a single blade, passage-to-passage variations were found in blade loading, shock positioning, and others, with some rotor outlet quantities displaying weak patterns in the circumferential direction in the tip and hub regions.

Contents

Chapter 1

Introduction

Computational Fluid Dynamics plays a key role in design of turbomachinery, with Reynolds-Averaged Navier-Stokes (RANS) simulations having become, in a way, the backbone of the industry. While these tools provide a reduction in both time and cost of component design, any discrepancy between simulation and reality can prevent results from being closer to actual experiments, which would further decrease reliance on real-life testing. Some of these discrepancies stem from the flow modelling itself, due to Reynolds averaging and the use of turbulence models for closure; on the other hand, the deviation between "idealised" geometries created in the design process and the component in operation can have a significant impact on flow quantities [1]. Adding to this, the variation can happen differently or with varying magnitudes between blade and blade, which can affect the flow in complex ways.

The present thesis is developed within the Institute of Gas Turbines and Aerospace Propulsion (GLR) at the Technical University of Darmstadt (TUDa), which over the years has conducted numerous experiments in a 1.5-stage transonic axial compressor within the Horizon2020-funded ARIAS project, to investigate forced response of a representative high-pressure compressor BLISK in an industry-relevant environment.
Through the use of Particle Image Velocimetry and unsteady pressure measurements, during experiments the presence of flow variations from blade to blade in steady-state conditions has been uncovered [2]. Blades displayed a difference in shock distance from the leading edge of more than five percent compared to the average at the peak efficiency operating point. Such a deviation is remarkable as this means every passage works at different operating points and has been proposed as a factor influencing the stability behaviour.

Based on this, the main objective of the thesis is to numerically investigate the effects of realistic geometry uncertainties on the flow in a transonic compressor and the impact on performance. To begin with, a reference single-passage domain is generated and simulated with commercial software and solvers, and later analysed. The rotor blade is subsequently parametrized, obtaining a flexible geometry which can be modified systematically by creating scripts that automatically modify the basic parameters of the geometry. The untouched parametrized blade is then compared to the standard configuration.
The scripts themselves present parameters to choose, each generating one kind of geometry modification. Sets of differing blades are then created, single-passage simulations are run, and results are compared to the default parametrized geometry. Finally, a full-annulus simulation is performed, where only one of the blades is different, featuring an increased stagger angle, with the objective of capturing blade-to-blade flow variations that extend beyond the single modified blade, as well as the interactions with the unchanged blades.

Another objective of this work is also to provide tools for future work on this subject. The blade modification script is designed to take simple inputs and generate an output that can be directly imported into the main CFD software used at GLR, unlocking the possibility of using external software to make a Design of Experiments for Monte Carlo simulations, for example. Finally, the domains set up in the process, especially the full-annulus one, are a useful stepping stone for future investigations.

Chapter 2

Literature review

Before diving into the process, it is useful to understand the causes and effects of these variances by looking at previous studies, as well as gain information in order to correctly model the systematic variations.

Geometric uncertainties have been a subject of study in the turbomachinery community for a long time, with Bammert and Stanstede [3] for example investigating experimentally in the mid-Seventies the effects of surface roughness and global thickness of blades in turbines as a result of manufacturing tolerances. The study used a four-stage air turbine to show the changes in mass flow rate, and the negative effects on enthalpy drop and efficiency when operating with "imperfect" blades in different configurations. Based on these, Balan and Tabakoff [4] inquired into the effects of particle erosion on compressor cascades and on an axial compressor stage experimentally, due to the performance deterioration of aircraft engines operating in environments with particle pollution such as sand. The differing performance was attributed to changes in the leading and trailing edges, tip leakages, roughness, and pressure distribution. Roberts [5], on the other hand, used a blade element panel method to conduct a numerical investigation on the effect of leading edge erosion, trailing edge angle, and stagger angle, and how a correct sorting and reshaping of blades is key to recover performance when overhauling the compressor. All of these studies are of paramount importance to the airline industry, due to the great impact even marginal gains in efficiency can have on the operating costs of an entire fleet of aircraft [6].

The more recent use of highly-accurate scans of turbomachinery blades and advancements in computation power has opened researchers to new possibilities. Through the

use of principal component analysis, Garzon and Darmofal [7] were able to characterize the variability in compressor rotor blade surfaces by reducing them to a few modes, and to use this in CFD simulations to obtain the statistical impact on the flow due to these modes, also finding that the greatest effect is caused by variation of the leading edge of the blade. While it was found that only six modes were needed to describe almost the totality of geometric scatter, these do not correspond to the known characteristics of a blade.
For this reason, Lange et al. [8] introduced a probabilistic model with parameters that are more intuitive, such as stagger angle, angle at leading and trailing edge, or thickness at leading and trailing edges. Therefore, these kind of parameters is what this thesis is based off of. A subsequent study by Lange et al. [9] set up Monte Carlo simulations to numerically investigate the sensitivity of the parameters in [8] (plus others) on efficiency and blade turning for example, showing a relative majority of the effects caused respectively by leading edge thickness and stagger angle.

Another kind of damage, other than erosion, can be caused by small foreign body impacts causing a deflection of the camber line at the leading edge as seen in Li and Sayama [10], also called "curl." A similar profile variability was also found in [5], however called "trailing edge tweak."
The work by Li and Sayama is also important in highlighting a different topic of research in this aspect of turbomachinery: namely, the effect of the presence of different blades within a rotor, closer to the topic at hand. This study looked at the variations on the flow near stall where, despite important differences in flow characteristics were found, the overall performance during stall was surprisingly not impacted. Similarly, the work from Venkatesh et al. [11] also inquired into the effect of tip gap change and localised erosion in a fan blade via CFD. The study looked into both the degradation of pressure ratio and efficiency, and that of the stall margin, then considered different patterns of damage around the rotor in the compressor map, and which are less detrimental to the previous quantities, finally considering the performance of fans with only some of the blades damaged.

Continuing on this topic, the contribution of Lu et al. [12] is worthy of consideration as it seems to be parallel to what is seen in the compressor rig at GLR as found in [2]. In this numerical study, a partially-coupled aeroelastic analysis is conducted to look into the phenomenon of alternate passage divergence (APD), where a single misstaggered blade is able to affect the whole rotor while in operation due to its variation of shock position affecting the loading of neighbouring blades, and hence their untwist behaviour, resulting

in an alternating pattern of stagger angle around the rotor. This behaviour, it was found, primarily affects the peak efficiency operating point, as it is usually the condition that divides a swallowed passage shock (towards choke) from an expelled shock (towards stall). That said, the magnitude of the phenomenon is heavily dependent on the blade's geometry, especially in the area called the "covered passage," corresponding to the area perpendicular to the chord line of a blade that overlaps with that of the neighbouring blade.
Finally, another study by Suriyanarayanan et al. [13] takes into consideration the change in stagger angle and tip gap between blades, with the first parameter causing again a change in the position of shocks affecting fan performance. As in [11], this one too focused on using patterns to mitigate reductions in performance.

To sum up, geometric variations in turbomachinery blades find their origin either in manufacturing, which can be due to factors such as internal strains, deformation of the processing system, tolerances, and manufacturing errors; or in operation as a result of particle ingestion and small foreign body impacts. The latter manifest mainly as erosion and curling, while the former can take a variety of shapes as shown in Tab. 2.1.

Symbol	Parameter
ax, tan	Axial and tangential position of section outline
λ	Stagger angle
c	Chord length
t_{LE}, t_{TE}	Thickness of leading and trailing edges
$pos_{t_{LE}}, pos_{t_{TE}}$	Assigned position on chord
t_{max}, w_{max}	Maximum thickness and camber of profile
$pos_{t_{max}}, pos_{w_{max}}$	Assigned position on chord
β_{LE}, β_{TE}	Angle at leading and trailing edge

Table 2.1: Geometric uncertainty parameters from [8].

Chapter 3

Methodology

The chapter presents the process followed throughout the work, with an initial description of the transonic compressor rig, the CFD tools, the setup, and then the mesh-independency study is introduced.
As the baseline configuration is created, the characteristics of blade parametrization and modification are described, as well as the selection of parameters reflecting geometric uncertainties that can be found on a typical rotor blade.

3.1 Case description

The TUDa-GLR-OpenStage (or "Open Test Case") is a single-stage configuration of the modular transonic compressor rig present at TU Darmstadt, representing the first stage of the high-pressure compressor of a typical commercial turbofan engine as described by Klausmann et al. [14]. It is comprised of a BLISK rotor with 16 blades and rotating nose cone, designed by MTU Aero Engines AG in the 1990s, a stator with 29 vanes designed jointly between the institute and the German Aerospace Center (DLR) featuring a 3D-optimized shape to reduce separation as shown in Bakhtiari et al. [15], and an outlet guide vane which is omitted in this study. The objective of this OpenStage configuration is to provide high-quality measurement data through the test rig to help the turbomachinery community improve numerical modelling of flows and validation. A schematic of the configuration can be found in Fig. 3.1.

The Open Test Case rotor, also named R1 as it is the first rotor that was tested, presents a tip radius of 190mm, a tip chord length of 94mm, and a tip gap during operation

of 0.8mm. The machine operates at a nominal speed of 20,000RPM with a mass flow rate of 16.0kg/s and a total pressure ratio of 1.50 at the design operating point (also called peak efficiency, or PE).

To tackle this study, the Ansys suite is used. In particular, DesignModeler and BladeEditor are used to create the geometric setup for the single-passage domains, while the meshing tool utilised to create the structured mesh is TurboGrid. Ansys CFX is the CFD solver for steady-state simulations, running the updated Menter k-ω Shear Stress Transport (SST) turbulence model [16]. The advantage of this model is the possibility to capture the boundary layer in more detail compared to k-ε models, but this comes at the cost of requiring a mesh that is highly refined in this region, reaching all the way down to the viscous sublayer. The solver uses pseudo time-stepping in the steady-state simulations to under-relax the flow equations, improving stability and convergence. More info can be found in its user guide [17].
Finally, the simulations are conducted first on a workstation equipped with an AMD Ryzen 7 3700X processor with 8 cores and 32GB of DDR4 RAM, and then on the Lichtenberg High Performance Computer (HPC), with the MPI section featuring a Linux cluster, each computing node possessing 96 processor cores (2x Intel Cascade-Lake AP) clocking at 2.3GHz, and 384GB of RAM.

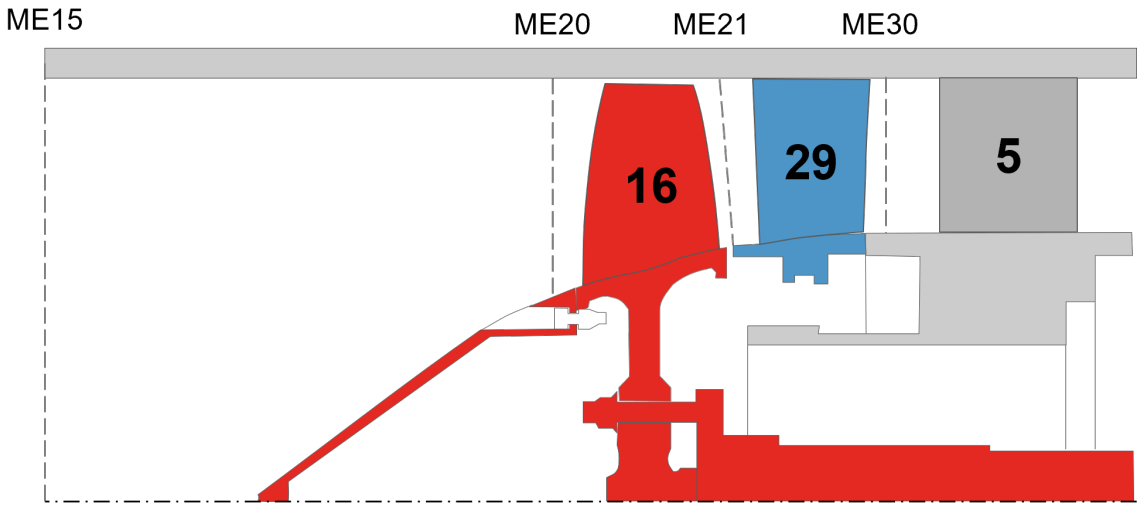

Figure 3.1: Schematic of the OpenStage configuration, including the OGV, with the experimental measurement planes.

3.2 Flow domain and meshes

All the tools are linked through Ansys Workbench modules. The general layout of a single-passage simulation in Workbench is shown in Fig. 3.2.

The first module is a DesignModeler one. In this, the geometry is imported:

- The rotor (R1) blades' hot geometry and stator (S7) vanes are imported as para-solids,
- The hub and shroud are imported as lines.

The latter dictate the length of the passage, with the inlet corresponding to the ME15 surface in the experimental rig, where the boundary layer rake is positioned, while the outlet is after the omitted OGV. This is done mainly to allow the flow to settle before the outlet boundary, aiding convergence.
Since the OpenStage configuration is simulating the front stage of a compressor, the nose cone would make the hub line reach the rotation axis of the machine, creating a wedge that is not possible to mesh. For this reason, the hub line is slightly "lifted" from the rotation axis to allow meshing. The nose cone does not feature the bolting holes in this study.

The hub and shroud lines are linked to create inlet and outlet lines and, finally, the translation of the geometry to TurboGrid for meshing is done by using the FlowPath tool of BladeEditor: this exports the blades and vanes as profiles at span heights decided by the user, in this case using 33 equally-spaced layers. When imported into TurboGrid, the profiles are united using B-Spline interpolation, obtaining a smooth geometry between layers, and this software also adds a tip gap as requested by the user. The running tip gap of the rotor is 0.8mm at the peak efficiency operating point, and this will be kept throughout the thesis. Keep in mind that, contrary to the real geometry, the rotor simulated here does not feature fillets, nor the hub gap between rotor and stator.

TurboGrid is used to generate the flow domain, the subdomains, and the grid. As stated before, fully-structured meshing is used so all of the domain presents hexahedra. The simulation of a single passage also means the program creates periodic boundaries automatically at the sides with the right pitch angles in order to have the correct number of blades and vanes in 360 degrees: 16 rotor blades and 29 stator vanes. In Fig. 3.3 the domain and its subdomains are shown: a first stationary inlet subdomain (S1) is present,

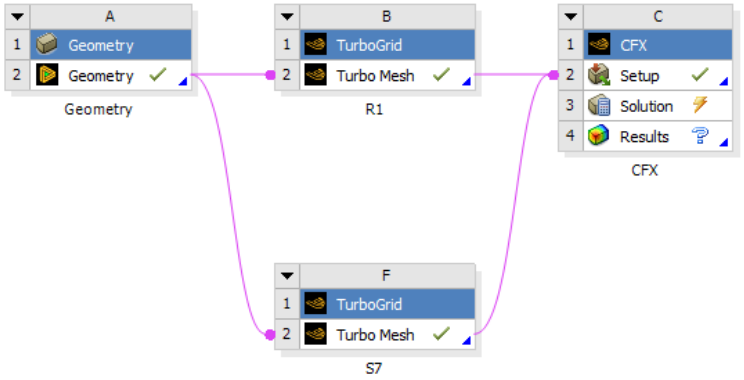

Figure 3.2: Workbench workflow for the standard single-passage simulation.

then the rotor (R1) with the nose cone follows, the stator (S7) then encompasses the stator vane and ends with the ”Stage outlet” surface, corresponding to the ME30 measurement plane in the experimental rig [14], finally an outlet subdomain extends the domain for improved convergence. The boundary conditions will be explained later on.

Using the SST turbulence model requires the first element to have an offset from the walls within the thickness of the viscous sublayer, meaning $y^+ < 5$. Dealing with a rotating machine, the thickness of the boundary layer varies greatly between hub and tip, and also between domains due to the presence or absence of rotation, resulting in necessary trial and error to achieve a suitable base mesh, which is then used to construct the more refined and/or coarser grids to compare to. Some details about the final meshes are summed up in Tab. 3.1.
The objective of the mesh independency study is not only, if possible, to achieve a grid that provides results as much as possible independent of the domain's discretization, meaning the refinement must be uniform in all directions, but also to estimate the error of such discretization. To do the latter, the Richardson extrapolation is used, which will later be explained in more detail, but this means refinements must be constant.

The software is not equipped with a simple parameter to use in order to scale the elements uniformly, with for example the ”Mesh Size” section only modifying the grid in the topology planes (2D) while other sections modify element density in a single dimension, and so a combination of values have been found to achieve the requested results as best as possible—meaning the elements are visually scaled uniformly and the mesh quality values are not changed significantly.

For the "Global Size Factor", which controls the density in the topology planes, a scaling factor of $\sqrt[4]{2.5}$ was found to be effective, while for the parameters that affect element size in a single dimension, $\sqrt[3]{2.5}$ worked. Examples of these latter parameters are the number of elements between hub and blade tip, and the offset of the first element from a wall.

Another remark is that, for all of the grids, the boundary layer elements on the rotor blade and at the blade tip present a target maximum expansion rate of 15%, while for all the other surfaces the maximums are between 20% and 30%.

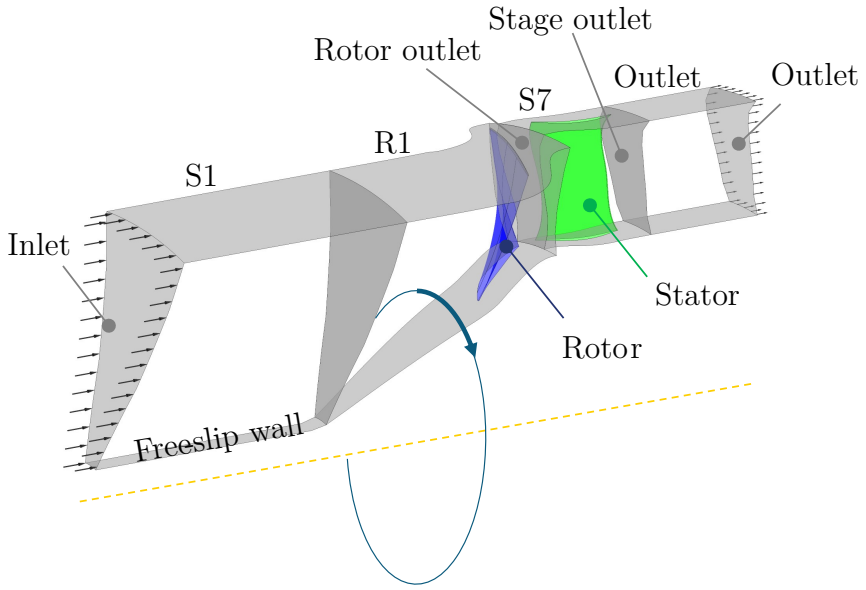

Figure 3.3: The single-passage domain used in the simulations, and its subdomains.

	Topology	Coarse	Base	Fine	Finer
Rotor	Global Size Factor	0.978	1.23	1.547	1.945
	Spanwise elements	72	96	129	177
	Elements in tip gap	24	33	45	61
	Axial elements in inlet domain	41	55	75	101
	Elements around LE at tip	9	12	14	18
Stator	Global Size Factor	0.636	0.80	1.006	1.265
	Spanwise elements	69	95	129	175
	Axial elements in outlet domain	22	30	41	55
	Elements around LE at shroud	8	11	13	16
Total	Elements (millions)	1.084	2.160	4.418	8.975
	Refinement	1.0	1.993	4.076	8.280
	Area avg. y^+	1.902	1.4041	1.0381	0.7653

Table 3.1: Details of the grids.

An example grid, the "Fine" one, is showcased in Fig. 3.4 for reference. Some edges in the topology have been refined, such as those at the leading and trailing edges, while others

were made coarser in order to reduce the overall number of elements. On this matter, the element count is quite large. This will impact mesh choice later on as the Lichtenberg HPC, while free to use, allocates for each project a set number of CPU hours, and the project this work was inserted into also had other people in it to share the allocated CPU time with.

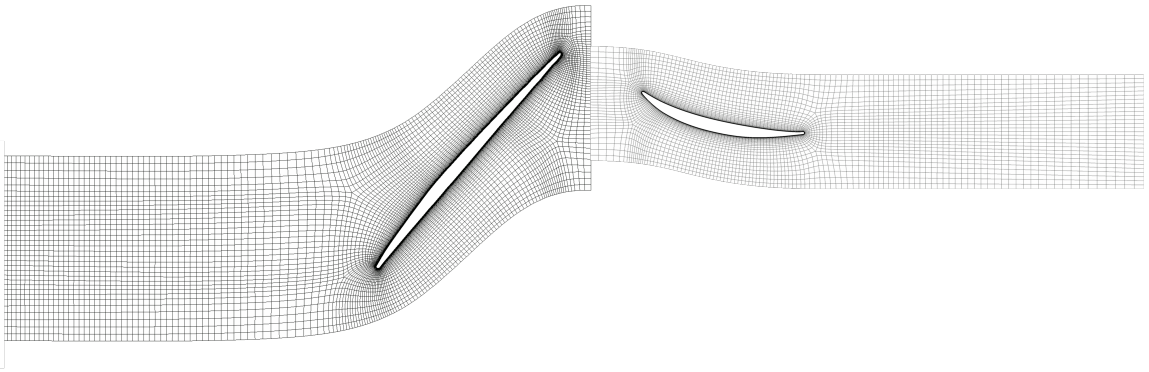

Figure 3.4: The Fine grid at 50% channel height, excluding the stationary inlet subdomain.

3.3 Simulation setup

Moving on, the simulation setup with its boundary conditions is here explained. The fluid used is "Air Ideal Gas", the Advection Scheme is set to High Resolution, while the Turbulence Numerics is set to First Order. Finally, the "High Speed Numerics" option is selected in the Advanced Options tab of the Solver Control, which is recommended for this kind of machine as it improves solver behaviour for high-speed flows, especially regarding shocks [18]. The inlet conditions are set as a purely axial flow with average total pressure and total temperature of 101325Pa and 288.15K respectively, and also with a turbulence intensity of 4% and a turbulence length scale of 0.09mm. These values come from the experimental rig itself at the same measurement plane.
The hub in the S1 subdomain, as it is representing actually the flow before the rotor cone and so does not present a boundary layer, is set to be a free-slip wall, while the shroud is stationary. The shroud is stationary in the whole domain (counter-rotating in the R1 subdomain).

The rotor subdomain is set as rotating, in particular throughout the study only the design speed of 20,000RPM will be used. The simulations are steady-state, so on the

inlet-rotor and rotor-stator interfaces, a mixing plane interface model is utilised, which performs a circumferential average of the flow through bands on the surface. Pitch angles are specified for the sides of the mixing-plane interfaces for correct averaging: S1 and R1 feature a pitch angle of 22.5 degrees, while the stator has a pitch angle of $360/29 \approx 12.414$ degrees.
S7 and Outlet subdomains are completely stationary, and the interface between them is a general connection one, without any mixing model in place.

The outlet surface regulates the machine's operating point (OP) by imposition of an average static pressure boundary condition, simulating the backpressure caused by the downstream throttle. As an example, the peak efficiency (PE) OP features a backpressure of around 131kPa. The imposition of P-total inlet and P-static outlet boundary conditions is considered more robust than the alternatives [18].

A few quantities were tracked in order to assess simulation convergence, along with the standard residuals, and mass and energy imbalances. These are the mass flow rate $\dot{m}$, the total pressure ratio π, and the isentropic efficiency η_{is}—these last two calculated between inlet and the "stage outlet" surface (ME30).
The mass flow is calculated at the inlet surface, and simply multiplied by the number of passages in 360 degrees; on the other hand, the total pressure ratio is calculated as

$$\Pi = \frac{p_{t,ME30}}{p_{t,in}}, \tag{3.1}$$

with the quantities on those surfaces being the massflow-averaged quantities. The total temperature ratio τ is calculated in the same way, resulting in the isentropic efficiency expression:

$$\eta_{is} = \frac{\Pi^{\left(\frac{\gamma-1}{\gamma}-1\right)}}{\tau - 1}, \tag{3.2}$$

where γ, the heat capacity ratio, is set to a value of 1.4.

Quantities, called Coefficients of Variation (CoV), based on $\dot{m}$, Π, η_{is} were used to ensure convergence of these. They were initially only calculated to monitor the convergence and see what values are to be expected, but were later used as convergence criteria themselves in order to make the simulations quit automatically at satisfactory levels of convergence.

Due to solution oscillation, instead of using the CoV of the quantity itself, defined as

$$CoV(\cdot) = \frac{\sigma(\cdot)}{\text{mean}(\cdot)}, \tag{3.3}$$

where mean$(\cdot)$ is the mean of the quantity over a set number of pseudo timesteps and $\sigma(\cdot)$ is the standard deviation over that same period, it was decided to use the CoV of the means, or

$$CoV(\text{mean}(\cdot)) = \frac{\sigma(\text{mean}(\cdot))}{\text{mean}(\text{mean}(\cdot))}. \tag{3.4}$$

In particular, mean$(\cdot)$ is taken over 150 timesteps, while the mean and σ of these are taken over 100 timesteps.

Finally then, the convergence criteria were set as follows:

- RMS residuals must be under 10^{-4},
- Mass and energy imbalance must be under 0.1% in all subdomains,
- The CoV of the means of $\dot{m}$, Π, and η_{is} must all fall under $2 \cdot 10^{-4}$ (only implemented after mesh study and compressor map calculation).

3.4 Mesh independency study

The meshes described in Section 3.2 are then simulated at an operating point close to peak efficiency, with an outlet static pressure of 131.0kPa. The choice of using this OP was made as this is usually the area with the best convergence over the compressor map. The quantities that are recorded for this are first the global quantities described before, being the mass flow rate in the machine, the total pressure ratio, and the isentropic efficiency, and also local quantities, these being blade loading at 95% and 50% of the span, and the circumferentially-averaged total pressure and total temperature ratios at the stage outlet.

The global quantities are used to obtain an estimation of the discretization error by using the method presented by Roache [19], based on the Richardson extrapolation, a

method also used in the study by Hansen et al. [20]. When a grid with spacing h outputs a solution Φ_h, the exact solution $\mathbf{\Phi}$ is

$$\mathbf{\Phi} = \Phi_h + \alpha h^p + H.O.T., \tag{3.5}$$

with α being a constant and p the order of convergence. The order of convergence can be obtained either by taking the logarithm of $\Phi_h - \mathbf{\Phi}$ from the previous equation and calculated as the slope of the curve formed by the data points if enough are available, with a regression, or by using three solutions with constant refinements:

$$p = \frac{\ln\left(\frac{\Phi_{2h}-\Phi_{4h}}{\Phi_h-\Phi_{2h}}\right)}{\ln(\lambda)}. \tag{3.6}$$

In Eq. 3.6, h represents the finest grid, $2h$ and $4h$ respectively the twice coarser and four times coarser meshes, finally λ is the (constant) effective refinement factor between successive meshes:

$$\lambda = \sqrt[3]{N_m/N_{m-1}} \approx \sqrt[3]{2}. \tag{3.7}$$

With Eq. 3.6 it is then possible to approximate the grid-independent solution and the discretization error ε_h^d as

$$\mathbf{\Phi} \approx \Phi_h + \frac{\Phi_h - \Phi_{2h}}{\lambda^p - 1} = \Phi_h + \varepsilon_h^d. \tag{3.8}$$

The results for the global quantities are shown in Fig. 3.5. Overall, a convergent trend is captured, with the values obtained being in line with other CFD studies of the OpenStage configuration, like the aforementioned Hansen et al., and He et al. [21], despite the lower total pressure ratio. This discrepancy is mainly due to the difference in the geometry, as will be explained later, and slight variations in the operating point as can be seen in the mass flow rate change in Fig. 3.5a. The challenge of grid studies is that each refinement is able to capture smaller and smaller flow features, which often results in decreased convergence performance, illustrated in Fig. 3.5c with the presence of non-negligible solution oscillations.

The resulting values are detailed in Tab. 3.2 and compared with the extrapolation

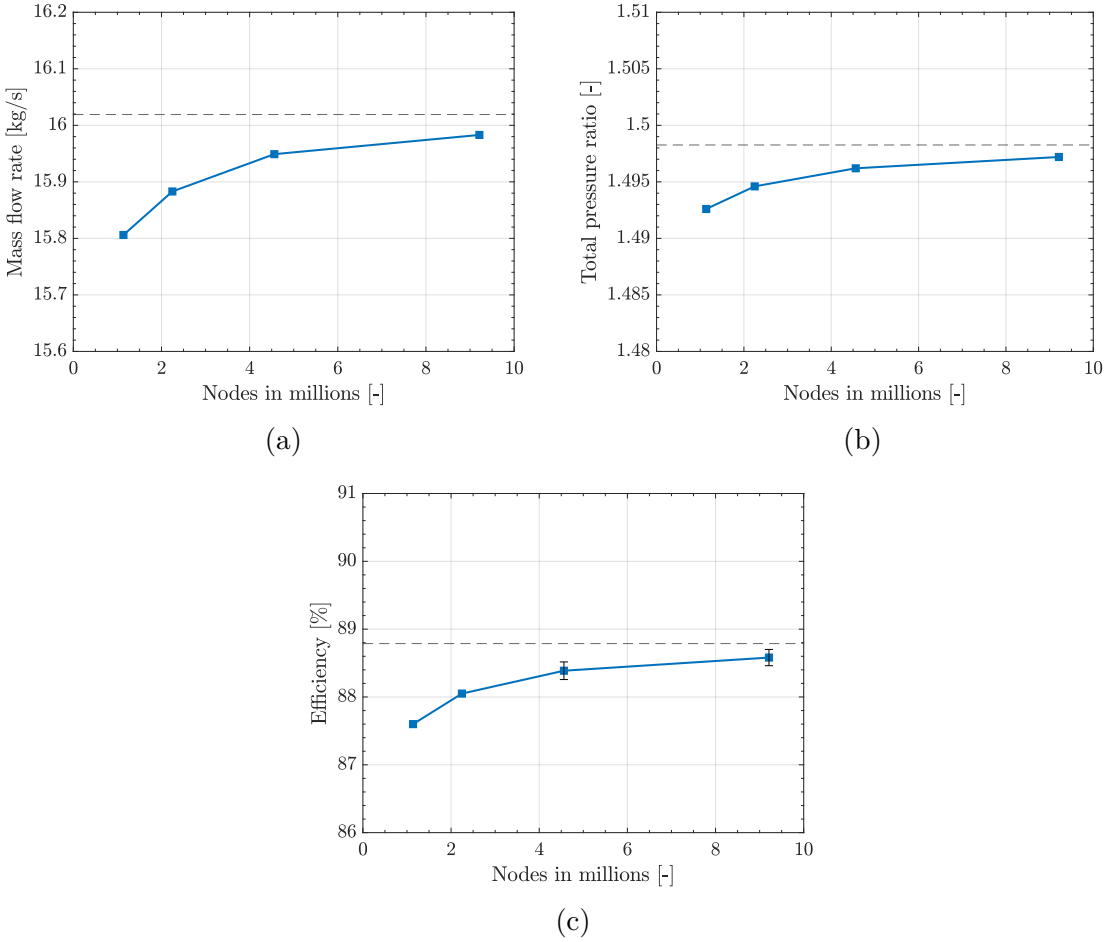

Figure 3.5: The mass flow rate (a), total pressure ratio (b), and isentropic efficiency with oscillation (c) for the four grids studied.

described before, where it can be seen that the approximated discretization errors for the Fine mesh are all under 0.5%, which is considered a satisfactory level of accuracy, with [20] reaching the same conclusion. Due to this and the CPU time allocated, the Fine grid is chosen for all the simulations taking place in this study.
The differences in rotor geometry that are going to take place are supposed small enough for them not to significantly impact the previous analysis on discretization errors. Therefore, the same parameters used to generate the Fine grid in TurboGrid are used to generate all the meshes without undertaking a new mesh independency study with each modification, reducing computation costs and time.

Moving on to the local quantities, these are used to assess the effect of mesh size on the flow fields. The circumferentially mass-averaged radial profiles at the stage outlet plane are shown in Fig. 3.6 for the total pressure and total temperature ratios, against the normalised span height. As can be seen, the profiles are very close between each other,

		Coarse	Base	Fine	Finer	Extrap.
Mass flow rate	Value [kg/s]	15.806	15.883	15.949	15.983	16.019
	Rel. diff. [%]	1.33	0.850	0.438	0.226	-
Total pressure ratio	Value [-]	1.4926	1.4946	1.4962	1.4972	1.4983
	Rel. diff. [%]	0.378	0.244	0.138	0.071	-
Isentropic efficiency	Value [%]	87.60	88.05	88.39	88.58	88.79
	Abs. diff. [%]	1.19	0.737	0.400	0.206	-

Table 3.2: Global quantities obtained with the various grids, compared to the extrapolated solution.

with the highest differences being in the total pressure ratio between 75% and 80% of the channel span, and the result of the Fine mesh overlapping with the Finer one. Adding onto the convergence of the solution, these are also similar to the ones found in [21], especially when comparing to the results with the shroud pinch at the rotor, which is present in this study. Such factor explains the lower total pressure ratio achieved compared to the aforementioned studies of the same configuration.

While these results are encouraging, it must be reminded that this measurement plane comes after the stator, therefore there is a damping of sorts caused by both the stator vane itself and the distance to the rotor domain—the mixing plane interface has been found not to significantly impact these spanwise profiles. For such reason there is a need for considering flow features in the rotor domain in order to better estimate the grids' performance, namely, the rotor blade loadings.

At 95% of the channel height, shown in Fig. 3.7, the pressure readings are similar, but show more differences: the suction side presents a sharp increase in pressure at around 60% of the axial chord, due to shock impingement, moving downstream, while on the pressure side near the leading edge there is variation of the initial slope. These differences are surely due to the difference in discretization error, however this behaviour might also be affected by the difference in operating points between the grids.
The result is that in this case the Fine and Finer grids are not overlapping completely.

At 50% of the channel height the situation is slightly different, as displayed in Fig. 3.8, due to the less extreme conditions. The curves vary mainly near the leading edge at the pressure side, and between 30% and 60% of the axial chord at the suction side, with the Fine grid overlapping the Finer one except for a small area near 40% of the axial chord.

Overall, the Fine mesh seems to present adequate performance to describe the flow

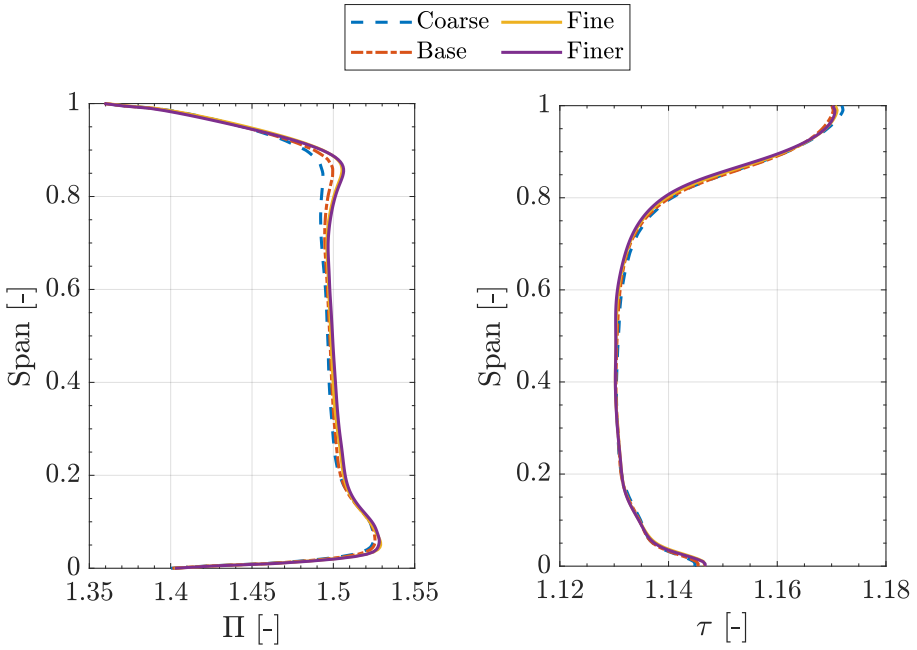

Figure 3.6: The total pressure ratio (left) and total temperature ratio (right) mass-averaged radial profiles at the stage outlet plane for the different grids.

features expected in this study.

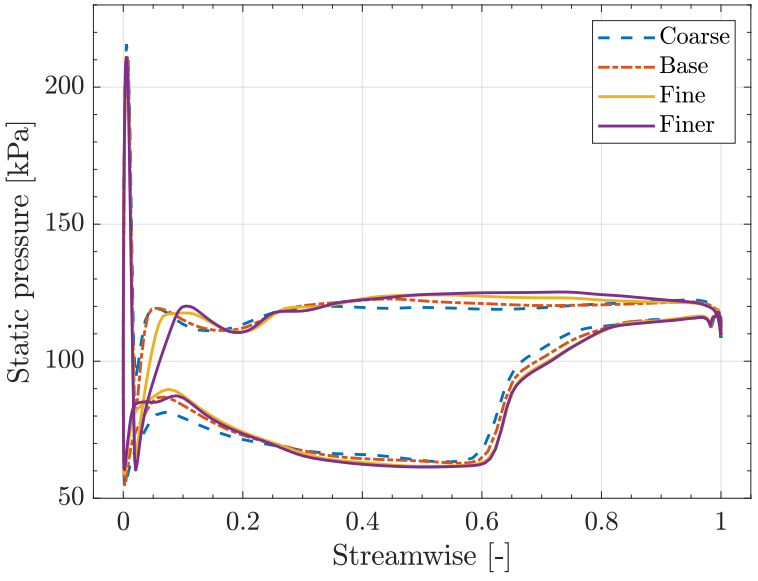

Figure 3.7: The blade loading profiles on the rotor for the different grids at 95% of the span height vs normalised axial chord.

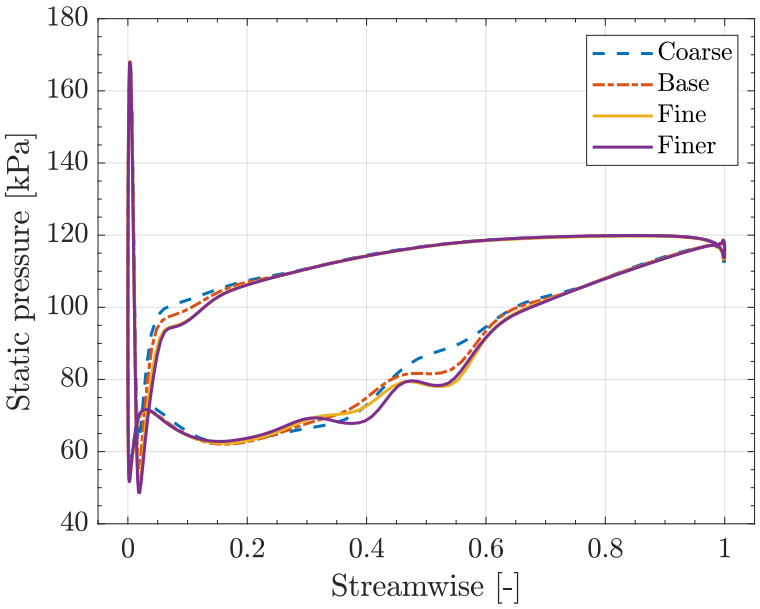

Figure 3.8: The blade loading profiles on the rotor for the different grids at 50% of the span height vs normalised axial chord.

3.4.1 Computational scalability

In order to efficiently use the computational resources provided by the Lichtenberg HPC, a study on the scalability is performed to assess the number of CPU cores to use for the simulations. CFD calculations can be easily run in parallel, meaning the flow domain is partitioned and sent to parallel processes that communicate between each other, however at one point the cost of communication between such processes becomes too high compared to the time it takes to complete an iteration, wasting the allocated computation time.

The setup consists in taking the chosen mesh, the Fine one, and running a small but constant number of iterations with increasing numbers of CPU cores parallelising the calculations. The solver time is then recorded and used to calculate the speed-up S_R, which is the ratio between the solver time and the one of the base configuration, featuring the lowest possible number of partitions (which is usually dictated by the memory needed by the simulation).

On the other hand, the ideal speed-up S_I is simply the ratio between the number of CPU cores used and the one of the base configuration. The computational efficiency is then calculated as S_R/S_I. The results are shown in Tab. 3.3.

It was decided that the lower limit for the efficiency would be around 75–80%, therefore, to reduce wall-clock computation time without sacrificing too much of the allocated

CPU time on the cluster, 30 cores should be used. However, these levels of efficiency can only be achieved when running three to four simulations at the same time (as is done when building the N100 speed line), as a user running a simulation with a fraction of a node will anyway lock the entire node for exclusive use, which is what finally counts in the allocated CPU time.

Cores	Ideal speed-up	Time for 11 iterations [s]	Speed-up	Efficiency [%]
5	1.0	576.2	1.0	100
10	2.0	300.2	1.919	96.0
20	4.0	167.6	3.438	85.9
30	6.0	123.6	4.661	77.7
40	8.0	101.2	5.695	71.2

Table 3.3: Scalability on the HPC for the Fine mesh.

3.5 Blade parametrization

The original hot geometry of the rotor blade is given as a parasolid object, therefore it can not be modified in a simple and automatic way to generate the geometry variations of interest in this study. The way to achieve this is to instead have the geometry divided into spanwise slices, with fundamental parameters that govern the generation of the final shape of each profile along the channel height.

Blade parametrization of the CAD blade is accomplished with two tools in the Ansys package: DesignModeler, with the BladeEditor module, and BladeGen. The advantages are that the parametrization is based on the previous setup, meaning it divides the blade with the same slices that are used in the FlowPath/ExportPoints feature, and that it is automatic. This ended up providing better results compared to other tested methods.

However, the process is not straightforward. To begin with, a ”CAD Import” feature is created, selecting the desired surface and FlowPath, as well as other parameters such as the use of Bezier or spline curves to build the profiles, and the type of leading and trailing edges. This creates a geometry feature that is the parametrized blade, however it is not a body and cannot be modified, but it can be exported as a Neutral Data File (.ndf). Such file is a parametrized geometry, collecting data on the blade profiles as well as the hub and shroud lines.

Possibly, since the resulting NDF files are quite large in terms of lines due to the

presence of the hub and shroud lines, featuring more than 20 thousand points each, the program is not able to import it. This and the somewhat difficult structure meant a different route had to be taken, so instead the file was imported into BladeGen. From here, the geometry can be modified, however the changes can be only made by dragging points and not systematically. The final step is then to export this as a BladeGen Batch Input (.bgi) file, which is an ASCII file that is easy to read and modify with external programs.

A BGI file has to finally be converted into a BladeGen Data file (.bgd) in order to be imported into DesignModeler, this can be done via a DOS command calling BladeBatch.exe. The powerful aspect of this is that the "Import BGD" feature of DesignModeler also creates a body of the new blade, meaning that replacing the original CAD body with the one now imported is all that changes in the DesignModeler module and the successive ones. Moreover, the body can then be used to evaluate any change done to the geometry compared to the initial one by using other CAD software or used in FEA.

To understand the process of modification, it is first needed to understand the contents of the BGI file which are, mainly:

1. Hub and shroud curves
2. Inlet and outlet curves
3. Leading and trailing edge curves
4. List of the layers and their normalised span position
5. Leading and trailing edge information
6. The meanline (or camber line) curves and type for each layer
7. The thickness curves and type for each layer.

Points 6 and 7 are the ones of most interest, as they play the main role in the blade's shape. These can be defined in a variety of ways but, for brevity, only what is present in the files of concern to this study is going to be described.

3.5.1 Coordinate systems and geometry

As explained for example in Siddappaji [22] and Nemnem et al. [23], various coordinate systems are used to construct a 3D blade from parameters. This information is needed both to understand how the modifications work and what is possible, and to visualize the changes through plots. The first coordinates are the cylindrical ones, r-z-θ, in which the first three features of the previous list are written, shown in Fig. 3.9.

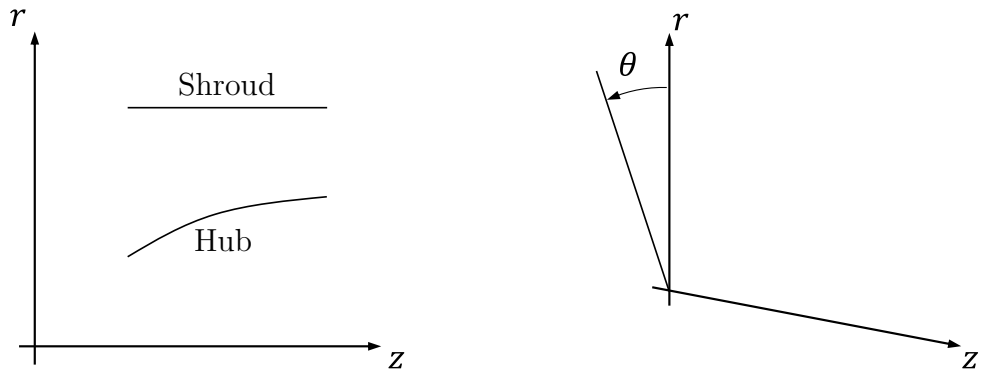

Figure 3.9: The cylindrical coordinate system used in blade generation.

In turbomachinery design it is needed to express the hub and shroud lines in this way as the airfoil construction is based off of a different coordinate system: in this case the m'-θ one, an angle-preserving space. m and m' are called meridional or streamline coordinates, and are a curvilinear coordinate corresponding to the curve with a constant percent height within the channel as described by the hub and shroud lines. A representation of it, along with a blade, is shown in Fig. 3.10, also implying that the airfoils are then curved in the r-z space.
In particular, m is the simple meridional coordinate, while m' is normalised by the average radial coordinate of the airfoil.

In the m'-θ coordinates, the airfoil is then constructed. Starting from the curve defining the meanline (or camber line) of the profile, this curve is created in the case studied from a series of control points defined in the BGI file and approximated via Bezier curves. The profiles always have the leading edge on $m' = 0$ as the position of the profile in the axial direction is controlled by the leading (and trailing) edge curves.
The profile itself is then generated by adding in the thickness information in the direction normal to the meanline for each m'. Just as before, this is a Bezier curve constructed from control points defined in the BGI file. An example of the two curves just described is in Fig. 3.11.

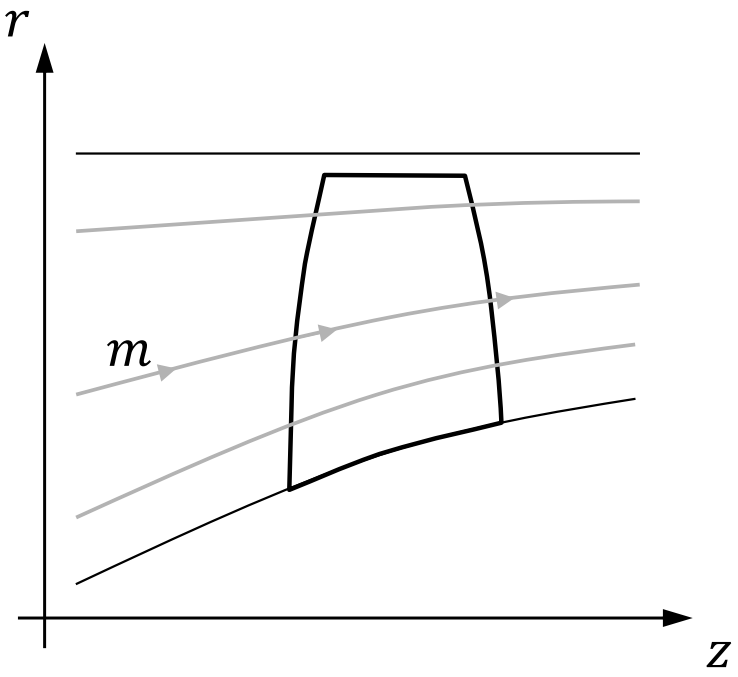

Figure 3.10: An example of the meridional coordinate as shown in the r-z space.

With this info, a profile can be created, as shown in Fig. 3.12. The leading and trailing edge information is provided in the BGI files simply as type, which in the case at hand is elliptical, and the ellipse's ratio at the hub and at the shroud, which in this case is equal to 1 (circular). Since it is not possible to provide localised information on these features, i.e. for each profile, they will not be studied, and therefore will not be shown in these representations.

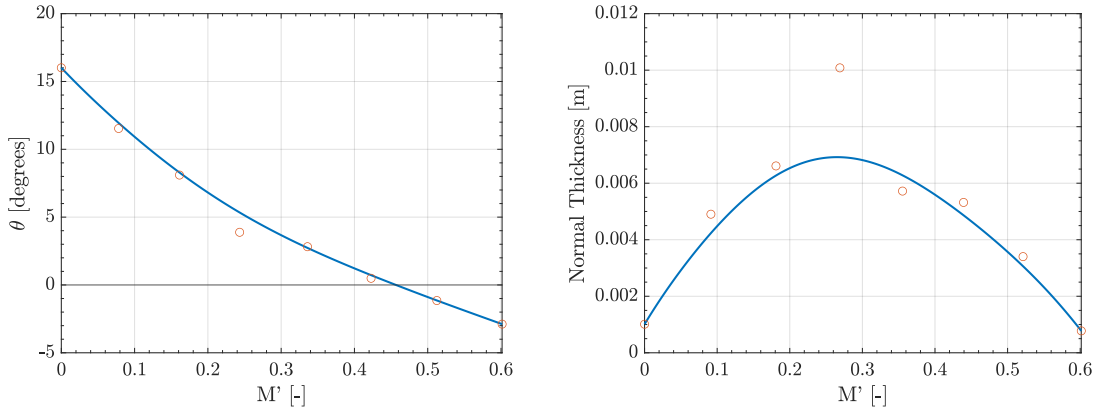

(a) (b)

Figure 3.11: An example of an airfoil's camber line curve (a) and thickness curve (b) created from the control points (in orange).

In the figure there are also some design features described: the angle between the constant θ line and the chord line is the stagger angle ξ; the metal angles β_{in} and β_{out}

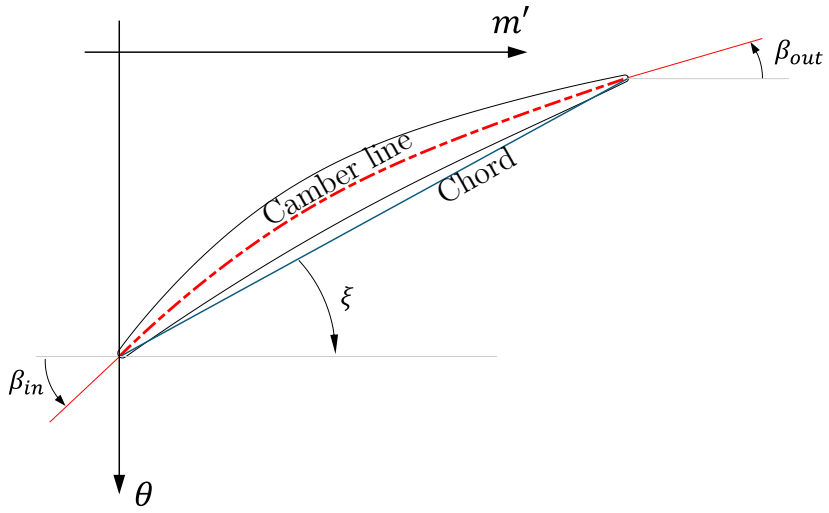

Figure 3.12: An example of a blade profile with camber line, note that the θ direction is positive downwards.

are the angles between the constant θ lines and the tangent to the camber line at the inlet and at the outlet respectively. These are highly important as they can regulate performance through flow turning, modifying for example the mass flow rate and loading of the machine.
Other quantities could be mentioned, such as the camber line angles, but they are not used in this thesis.

The angles shown in Fig. 3.12 are each represented pointing towards the positive direction.

By generating multiple profiles, they can be stacked in the radial direction to create the 3D blade. The stacking can be performed in different ways, such as on the leading edge, trailing edge, at the centroid of the airfoils, and offsets can be included in axial or circumferential directions, providing respectively sweep and lean of blades. Here the stacking is only controlled, in the axial direction, by the leading and trailing edge curves, while in the circumferential one it is controlled by the camber line.

3.5.2 Geometry modification

As described in the previous section, the blades' profiles in the BGI file are defined by the control points of the camber line and of the thickness line. These, along with the control points for the leading and trailing edge curves, are what can be controlled to change

the geometry. What is then necessary, is to identify the blade modifications that are of interest, and create scripts that can use simple inputs to modify all those parameters to reproduce such changes in the final blade.

Back in Chapter 2, it was seen that there are a series of geometric uncertainties that have been found in previous studies, either produced by wear in operation or in manufacturing and assembly. Most of these, but not all, were summarised in Tab. 2.1, and now the procedure of applying these changes is going to be exposed. The pictures in this part are only used to better understand how the modifications work, so they are of a much bigger scale compared to realistic geometric uncertainties found in compressor blades.

A first major group of modifications is that of the leading and trailing edges' camber line. The first control point of the curve can be moved up or down in the θ direction, corresponding to a circumferential motion of the first part of the profile, changing the metal angle β_{in}. Consequently, this will also modify the chord length and the stagger angle, while maintaining the axial chord length. An example of this change is shown in Fig. 3.13a in the positive direction, meaning the position θ of that point gets moved to more positive values. The same considerations are valid when modifying the last point of the curve, the trailing edge of the profile. These changes of the control points correspond one-to-one to the shift of the curve as they are the first and last points of the Bezier curve.

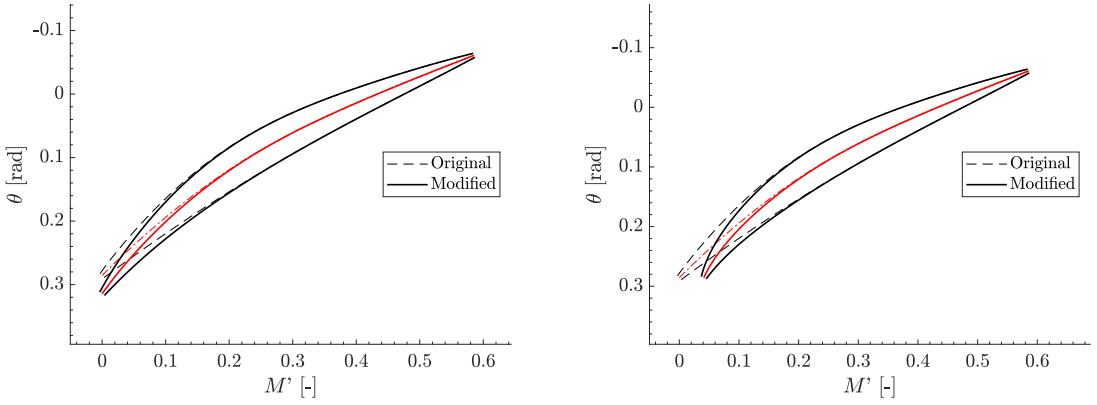

Figure 3.13: Leading edge camber line shift in the circumferential (a) and axial (b) directions.

On the other hand, modifying the leading and trailing edge curves for a layer in the BGI file means moving these points in the axial direction, an example of which is displayed in Fig. 3.13b, with a positive change of this parameter being the motion of the

point towards more positive axial values—i.e. downstream. This will again modify both the stagger angle of the profile and the chord length, as well as the axial chord length. The modified profile in the picture is aligned to the trailing edge instead of the leading edge of the original to visualise what actually happens to the blade instead of what is written in the file.

While the previous can be considered a curl, as found in [10], it only works in the positive direction, and vice versa for the circumferential shift. A specific curl parameter is instead created in this study such that it works in both directions easily and compounds an angle change of the first (or last) point with a shift in the axial direction of it that preserves the chord length c of the profile. The challenge of this modification is that the leading edge control point has to stay at $m' = 0$. The process goes as follows:

1. The camber line point with $\theta_{LE,1}$ is shifted in the circumferential direction to $\theta_{LE,2}$
2. The overall change is treated as a rotation of the chord line around the trailing edge, so the new stagger angle is found as

$$\xi_2 = \arcsin\left(\frac{\theta_{LE,2} - \theta_{TE,1}}{c}\right) \tag{3.9}$$

3. The difference in axial chord $\Delta m'$ in the m' direction is computed from the new stagger angle
4. $\Delta m'$ is converted to the unit of the axial coordinates, and the leading edge point of the layer is shifted accordingly by that amount
5. Except the first, all the control points in the camber line and thickness curves are shifted in the m' direction by $\Delta m'$.

An example for the leading edge modification near the tip of the rotor is shown in 3D in Fig. 3.14. The process for the trailing edge is almost the same, however this time the change of the control point is calculated as a rotation of the chord line around the leading edge, and the meridional difference $\Delta m'$ is only applied to the control point that is being modified instead of all the others, since this point is not constrained to a particular value. Finally, point 4 of the previous list is done but on the trailing edge curve instead.

A second group of changes is the one regarding thickness, which was found in [9] to be the main factor impacting efficiency. Therefore, three modification parameters are

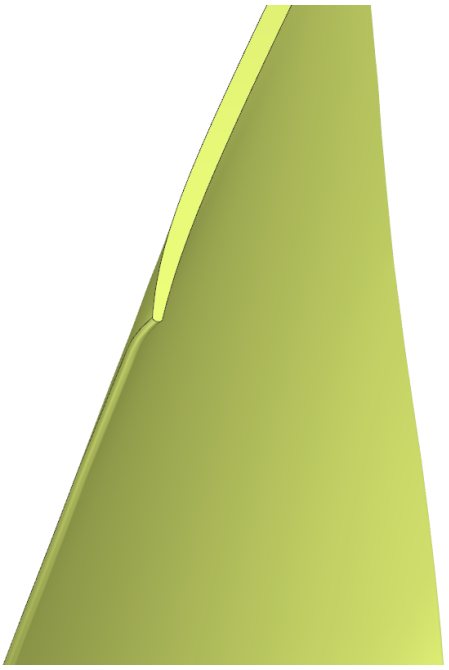

Figure 3.14: A blade with added LE curl at the tip.

created: leading edge thickness, trailing edge thickness, and maximum thickness.
The first two are simply implemented by modifying the first and last control points of the thickness curve of the file, again because they correspond one-to-one to the shift in the first and last points of the Bezier curve built from them. The same is not true for the maximum thickness modification: a 10% change in the highest point of the thickness curve causes a lower actual change in the point of maximum.

The modification is not applied to a single control point, but is spread to various points except the leading and trailing edge ones. A distribution is created such that the control points feature a change given by the corresponding evenly-spaced points of a $C \cdot \sin^4 x$ curve, with $x \in [0, \pi]$. C is the chosen amount of modification.
A Bezier curve of these new thickness control points is built and error between the new maximum value and the requested value is calculated. Until this error is not smaller than 1% of the requested change, a simple bisection method is used to iterate towards the final value.

The method does not take into consideration the initial shape of the thickness curve, and while for the case studied it is valid to use for lower layers, which present thickness curves similar to a sinusoid between 0 and π, the closer to the tip, the more the curves become flat. This means that in the top layers the position of the maximum could be shifted significantly.

The penultimate group of changes, the general camber line modifications, only includes one parameter in the present study, this being the stagger angle change. Other parameters were considered, such as the shift of the whole profile in the axial and circumferential directions (sweep and lean), however they were not found to have a great impact in [9], and no other studies were found suggesting otherwise.
The stagger angle change is applied to the whole blade with the same amount, and the modification process of a layer starts with a rotation of the camber line curve around a point specified by the user (as a percentage of the axial chord of the hub layer of the blade). From there, the points are shifted axially to have the leading edge at $m' = 0$. The total shift for each control point is recorded and applied to the control points of the normal thickness curve to have a matching profile. Finally, the difference in meridional position between original and modified leading and trailing edges (before the final axial shift to have the leading edge at $m' = 0$) is converted and applied to the axial position of the leading and trailing edge curves.

The result is that the stagger angle is changed around a single axis, and this axis can be chosen by the user as shown in Fig. 3.15. A positive variation of stagger angle is considered as an increase, leading to a decreased incidence angle.

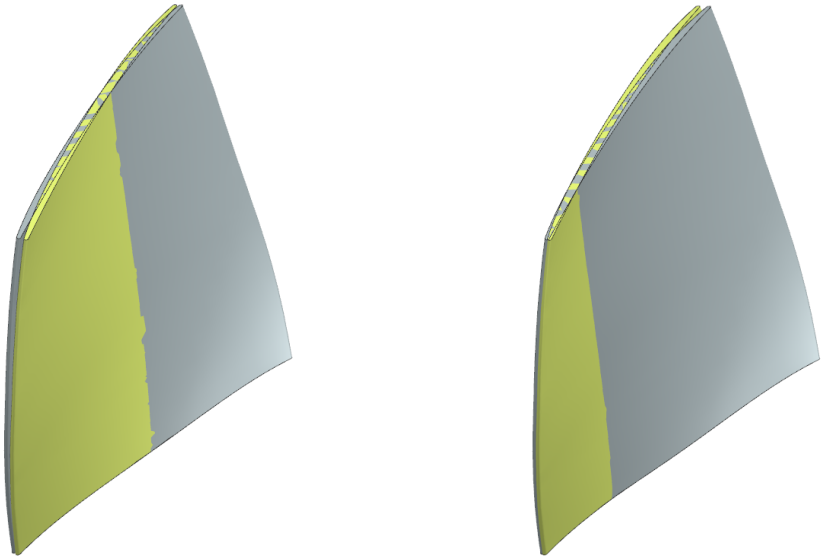

(a) (b)

Figure 3.15: Blades with modified stagger angle rotating around the midchord point (a) and around 25% of the chord (b) of the bottom layer.

Finally, the only parameter that is not modified with scripts but from within Ansys is the tip gap. The blades used in the study are always overextended to intersect the hub and shroud and use the FlowPath feature of BladeEditor. If this was not the case, which

happens when modelling the flow volume instead of letting it be generated by TurboGrid, the tip gap could have been implemented into the 3D blade instead.
Therefore, this parameter is chosen from within TurboGrid when creating the mesh, and a positive change is defined as an increase in tip gap.

Overall, the blade modification parameters have been described and are listed with some more information in Tab. 3.4. Note that, for some, the order of modification matters, as applying a curl to the leading edge and then subsequently varying the circumferential position of this point is not the same as doing the inverse. This is due to the nature of the modifications, the use of relative variations instead of absolute ones, and also because an exemplary unifying script was created that applies the various modifications in sequence, so one on top of the other, with the input being an array where each row is one of the blade's layers and the columns are the various parameters to change. For this study this aspect is not a concern since only once will more than one parameter be changed, however it is important to keep in mind when generating blades for Monte Carlo simulations in the future.

Parameter	Description	Quantity change
θ_{LE}, θ_{TE}	θ position of LE and TE	Percentage of original θ_{LE} or θ_{TE}
ax_{LE}, ax_{TE}	Axial position of LE and TE	Percentage of original axial chord
$curl_{LE}$, $curl_{TE}$	LE and TE curl	Percentage of original θ_{LE} or θ_{TE}
t_{LE}, t_{TE}	Thickness of LE and TE	Percentage of original thickness
t_{max}	Maximum profile thickness	Percentage of original maximum thickness
ξ; pos_{ξ}	Stagger angle and point of rotation	Percentage change from original ξ of the blade's bottom layer; position on bottom layer's normalised axial chord
$tipgap$	Tip gap	Absolute

Table 3.4: Geometric uncertainty parameters.

3.6 Full annulus setup

In line with some of the recent research in the topic, as explained in previous chapters, one of the objectives is to find a way to set up a full-annulus simulation within Ansys where the machine features a single modified rotor blade, while all the others are kept standard. The set up was intended to not alter the initial workflow by much, the reasoning being twofold:

- While simpler to create, using a fluid volume would mean including a new mesh independency study on the configuration, and possibly having to alter the base blade parameters to feature tip gaps;
- The workflow used until now is standard practice in the GLR, changing it would mean additional time spent learning all the aspects of a new framework, also by future users.

The challenge with such a task is that TurboGrid generates single-passage domains independently, as this program was not made to have differing blades, but to have the same one that can be repeated for multi-passage simulations (with periodic surfaces) or full-annulus simulations. Therefore, modifying a blade's shape results in a change in the periodic interfaces between the blades, so two different blades will present intersecting interfaces and/or gaps.

What was found to be a valid approach is to have the modified blade be meshed considering a higher number of blades in 360 degrees compared to the standard 16. This way the program creates a narrower passage domain that does not intersect the neighbouring ones, instead featuring quite large gaps. The mesh for the modified blade is then saved. The previous workflow is kept, with the standard rotor subdomain R1 inside CFX being repeated 15 times around the rotation axis, while the other subdomains are repeated to have a full-annulus configuration (16 for the inlet subdomain, and 29 for the stator and outlet ones). The modified blade subdomain is inserted in the remaining space.

A single iteration of this is run, and used to extract the periodic surfaces of the standard "R1" subdomain and of the modified "R1mod" subdomain. These surfaces are imported into ICEM and used to create a "gap domain" for each side of the modified blade, which act as bridges between the R1 and R1mod subdomains. To do so, the aforementioned surfaces are used to build the inlet, outlet, hub, and shroud surfaces. An

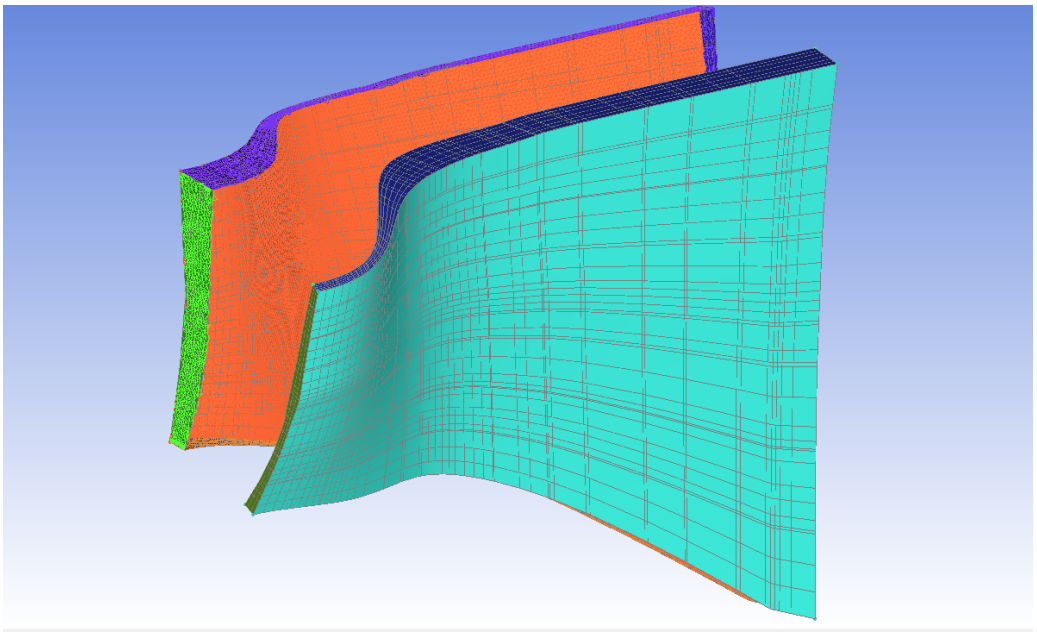

Figure 3.16: Example of the volumes built in ICEM to bridge the gap between standard and modified rotor subdomains, seen from downstream and above the rotor.

example of the two volumes as seen from downstream of the rotor are displayed in Fig. 3.16 and, between them, the modified blade will be positioned.

Time restrictions and inexperience with the software meant the meshing of the gap domains was not studied as thoroughly as the standard one. The final grid is an unstructured one featuring 10 layers of prismatic elements at the hub and shroud surfaces each to capture the boundary layer, with a growth ratio of 1.15. The two bridge domains have a total of around 660,000 nodes, and one of the two is displayed in Fig. 3.17 looking from upstream of the blade.

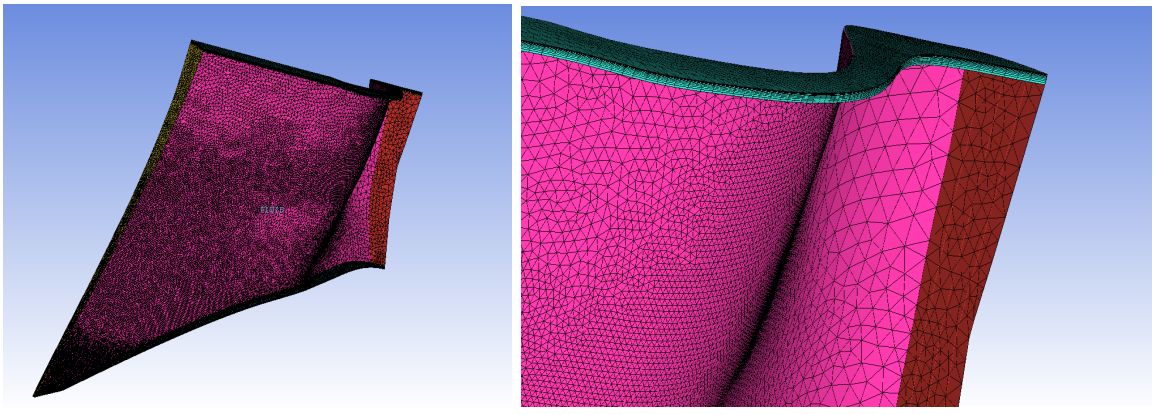

(a) (b)

Figure 3.17: One of the gap domains meshed (a) with a zoom on the prism layers at the shroud (b), seen from upstream of the rotor.

The meshes are finally saved and imported into the CFX module with all the other components. The downside of the chosen method is that gap domain generation is not automatic as the periodic surfaces, which also change with each blade modification, have to be exported, with all the other surfaces being based on them.

Correctly setting up the interfaces is the only task remaining.
First the periodic interfaces separating the various rotor domains are removed and substituted by general connection interfaces without transformations inbetween ("None"). This way, the fluid is able to travel between modified rotor, gap domains, and standard rotor domain one-to-one, just as it does for example in a tip gap interface.
Another change is that the mixing-plane interface between S1 and R1 now encompasses both the inlet surfaces of the R1 subdomain as well as those of the R1mod and gap subdomains. The same thing is done for the mixing-plane between the rotor and the stator by including the outlet surfaces of the aforementioned subdomains. This way the averaging is performed correctly around the annulus, with a pitch ratio of 1, meaning both sides span the same angle of 360 degrees.

Finally, the computational scalability of this mesh on the HPC was studied as well with varying number of nodes, recording the solver wall time needed for six iterations to be completed. The results are shown in Tab. 3.5, according to which four nodes are chosen to be used in order to reduce the "wasted" CPU time for this large simulation featuring 84 million elements.

Nodes (cores)	Ideal speed-up	Time for 6 iterations [s]	Speed-up	Efficiency [%]
2 (192)	1.0	402.9	1.0	100
3 (288)	1.5	267.0	1.5	100
6 (576)	3.0	168.4	2.4	79.7

Table 3.5: Scalability on the HPC for the full-annulus simulation.

Chapter 4

Results

In this chapter, the results of all the performed simulations are going to be shown, starting with the solution of the standard CAD blade, then moving to the performance of the parametrized geometry and its differences with the CAD one, then explaining the single-passage simulations performed with sets of modified blades, each with a parameter changed, and how the flow is affected.

4.1 CAD geometry and speedline

The result of the mesh independency study leads to the analysis of the solution for the CAD geometry with the Fine mesh. Reiterating the global quantities found: the mass flow rate is 15.95 kg/s, which is adequately close to the design point of peak efficiency of the machine (16.0 kg/s), the total pressure ratio between inlet and stage outlet is 1.496, and the isentropic efficiency is 88.39%.

To start off, the blade loading is shown again but only for the chosen mesh in Fig. 4.1 at 95% of the span height. In this it can be seen the initial spike in pressure of the stagnation point, decreasing and then separating into the pressure side and suction side of the blade. The pressure side still presents an area with a high velocity almost matching the one on the suction side, due to the leading edge shape and flow angle.
While the pressure side is somewhat constant in pressure, the suction side presents a noticeable increase in pressure after 60% of the axial chord occurring at a high rate of change, suggesting the presence of a shock. Indeed, this is what is found when looking at Fig. 4.2, where the Mach number at 95% of the span is displayed on a blade-to-blade

plot. The bow shock of the neighbouring blade impinges on the suction side of the blade around that area, also creating a separation area with low velocity. Keep in mind that in all the blade-to-blade plots, the flow goes from left to right, and the machine's tangential velocity vector points downwards.

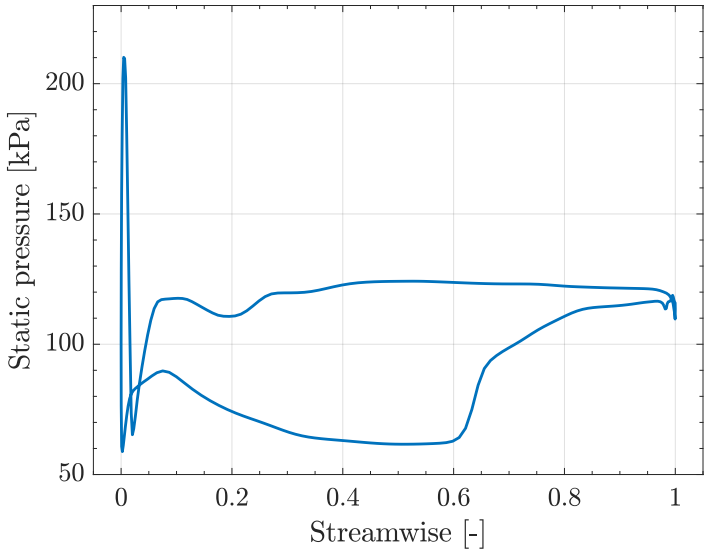

Figure 4.1: The blade loading on the rotor at 95% of the span height vs normalised axial chord.

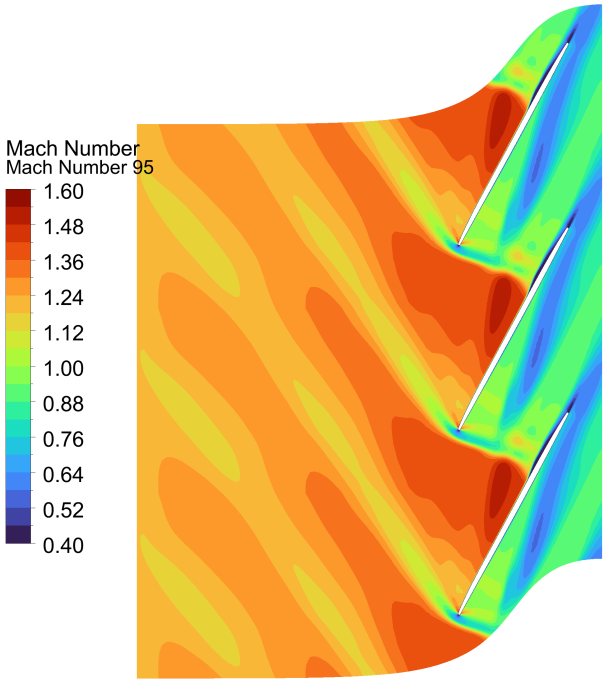

Figure 4.2: Blade-to-blade plot of the Mach number at 95% of the span height.

The plot also highlights the tip leakage vortex, being the low velocity area travelling

downstream towards the trailing edge section of the following blade. It is possible that the tip leakage vortex, in conjunction with the separation area after the shock impingement, create a blockage area in the passage that slightly accelerates the fluid back above Mach 1.

Outside of this tip area, nothing worthy of remark is present in blade-to-blade plots, so these are omitted for brevity.

A useful picture is the surface streamlines on the blade, seen in Fig. 4.3. These provide an overlook of the flow over the rotor blade and hub, akin to what is done experimentally with oils, making it possible to visualize the path of the flow over the blade, as well as phenomena like separation and recirculation.
The findings here are in line with the peak efficiency SST results of He et al. [21], and are as follows: the shock impinging on the blade's suction side (red line) becomes strong enough near the tip region to cause separation of the flow, followed by a reattachment which moves downstream when getting closer to the tip, barely reattaching at 95% of the span. Down below, the hub corner separation is captured. Near the trailing edge in the hub region a recirculation area is present, and finally there is the cross-flow at the hub caused by the higher pressure fluid of the following blade's pressure side going towards the suction side.

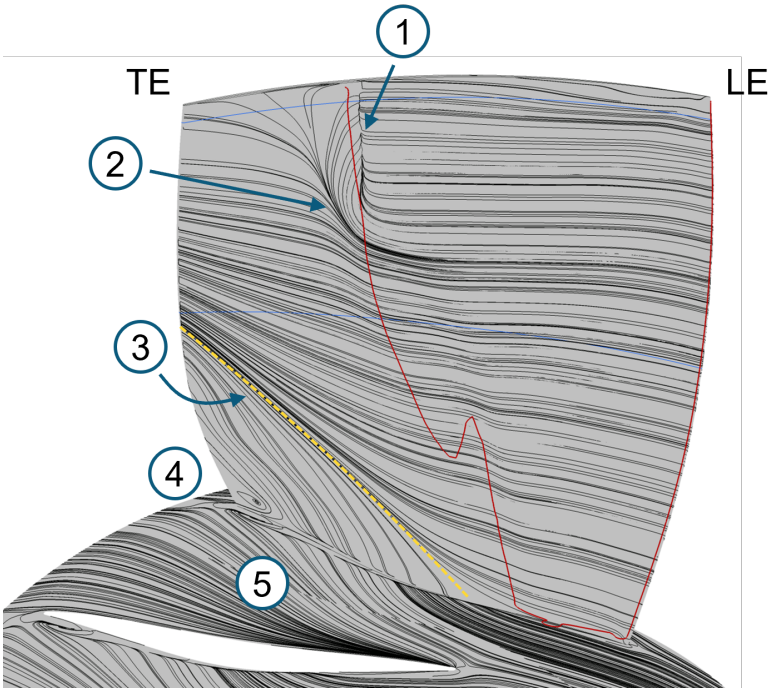

Figure 4.3: Surface streamlines on blade suction side and hub, with reference lines indicating Mach 1 (red), and 50% and 95% span heights (blue). ① shock-induced separation, ② reattachment line, ③ hub-corner separation line, ④ recirculation area, ⑤ cross-flow.

Note that the red line indicating the regions where Mach equals 1 is only used as a reference and is not an absolute value, since it is built by taking the areas with such flow velocity at an arbitrary distance from the wall (and removing the values at or above the tip). Despite this, the position is fairly accurate when compared to profiles of the isentropic Mach number at various span heights calculated from the local pressure on the blade.

Moving onto other characteristics, in Fig. 4.4 the total pressure at the rotor outlet is shown in the relative frame of reference; the view is from upstream of the rotor. Here the tip flow vortex is visible as the area with the lower total pressure towards the tip, the horizontally-elongated shape being due to the vortex coming at an angle towards the surface. The wake is also visible, the thin part near the hub seemingly caused by the flow climbing area below the hub-corner separation line, and the recirculation zone, with more energetic flow instead coming from the rest of the passage.

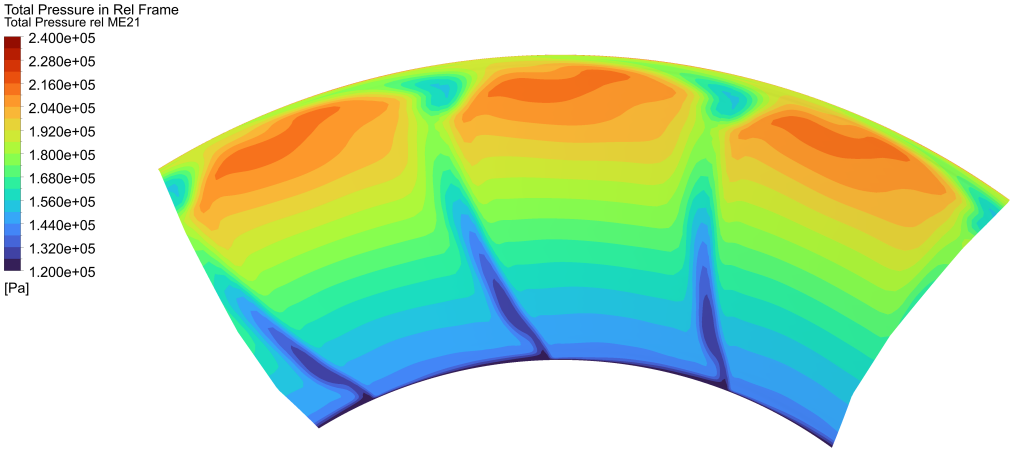

Figure 4.4: Total pressure in the relative frame of reference at the rotor outlet.

By changing the outlet static pressure boundary condition of the configuration, it is possible to change the operating point along the design speedline (N100) of the machine: a higher backpressure increases the blade loading, going towards stall conditions, while a decreased backpressure will let the machine approach choking conditions. The outlet static pressure has been changed with varying steps of a few kPa usually, decreasing down to 300Pa towards the stability limit in the stall region.

Fig. 4.5 shows the resulting speedline in terms of total pressure ratio and isentropic efficiency. Note that, in parallel to what happens in the other studies, the numerical speedline does not reach as far into the stall region as the experimental data, since nu-

merical instabilities arise especially due to the onset of unsteady flow phenomena, which cannot converge in a steady RANS simulation. The last converged point is just under 14.5 kg/s.

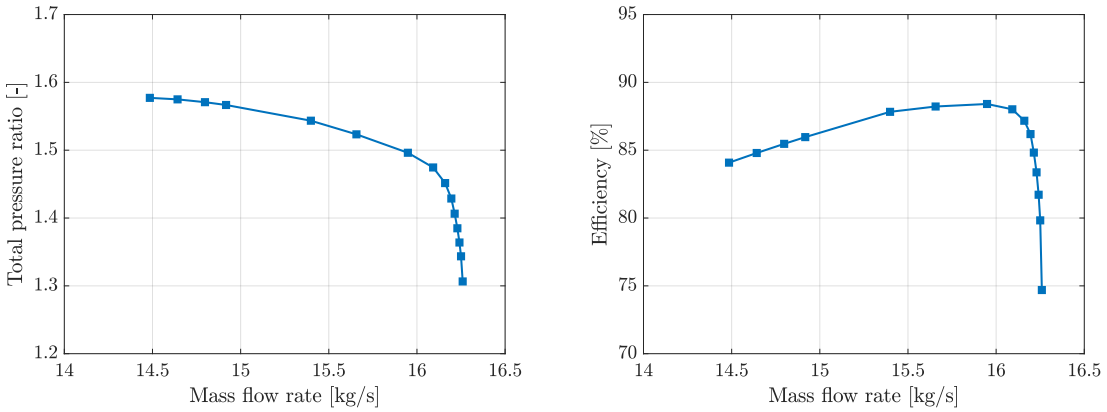

(a) (b)

Figure 4.5: The N100 speedline (a) and corresponding isentropic efficiency (b).

4.2 Parametrized geometry

With the baseline CAD geometry analysed in its resulting flow, the parametrized geometry resulting from Section 3.5 is compared to it in order to assess the accuracy of both the geometry and the changes in the flow resulting from these variances.

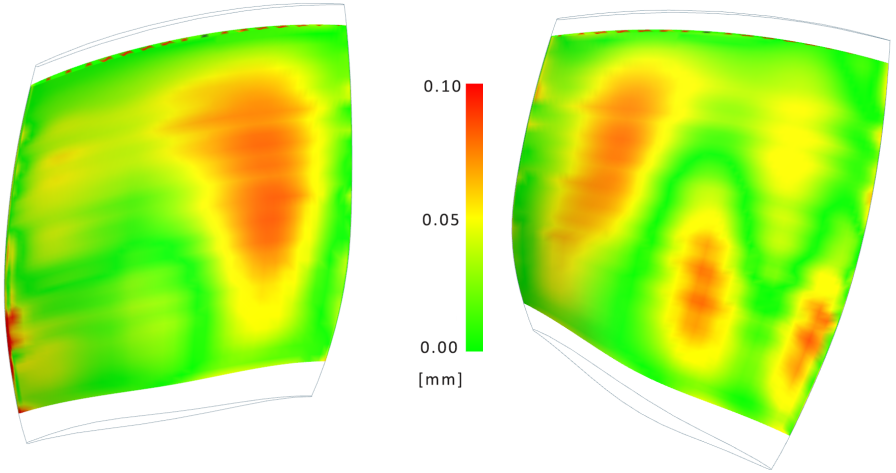

(a) (b)

Figure 4.6: Absolute geometric deviation between CAD and parametrized blade, pressure side (a) and suction side (b).

The geometric deviation between the two blades is calculated with the "Deviation Gauge" feature of Siemens NX, and shown in Fig. 4.6. The CAD blade is the outlined one, extending further in the radial direction compared to the parametrized one. It has been found that the maximum difference between the two blades is achieved at the leading edge of the blade at around 25% of the span, at 0.146mm. While it could look like a small variation, the fact that it is located on the leading edge might be a concern as it is a critical area that could change the flow significantly. To put it into perspective, this area of the blade features a leading edge diameter of around 1mm, so this thickening changes the diameter by more than 10%.
The rest of the blade's variations are under 0.1mm, peaking around 0.08mm. These changes could be within the same order of magnitude of the real blade's geometric uncertainties.

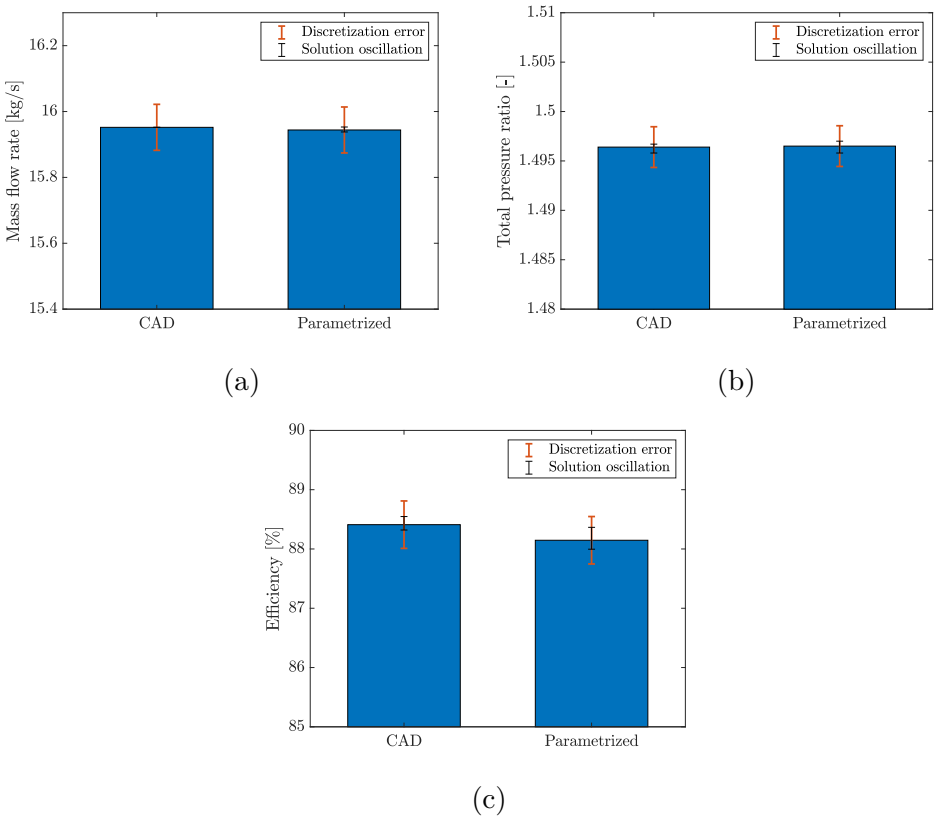

Figure 4.7: The mass flow rate (a), total pressure ratio (b), and isentropic efficiency (c) compared between the CAD blade and the parametrized blade.

This new geometry is then used to run the same simulation as before, at the same operating point near peak efficiency, with the same input parameters for the grid generation, so that any variation is due to the new geometry. Starting with the global quantities, in Fig. 4.7, the results are shown including the oscillation of the quantity of interest, and the

approximated discretization error as calculated in the mesh independency study. Change outside of solution oscillation is still considered meaningful even if inside the discretization error area, as first of all the tested geometries are different and might feature a different approximation of the error, and also the sensitivity might be correct provided enough resolution. Therefore, this value should only be looked at for reference, both here and in the subsequent section.

The global quantities are found to all be within solution oscillation, indicating that the present set up is virtually unaffected by the geometric variation caused by the parametrization.

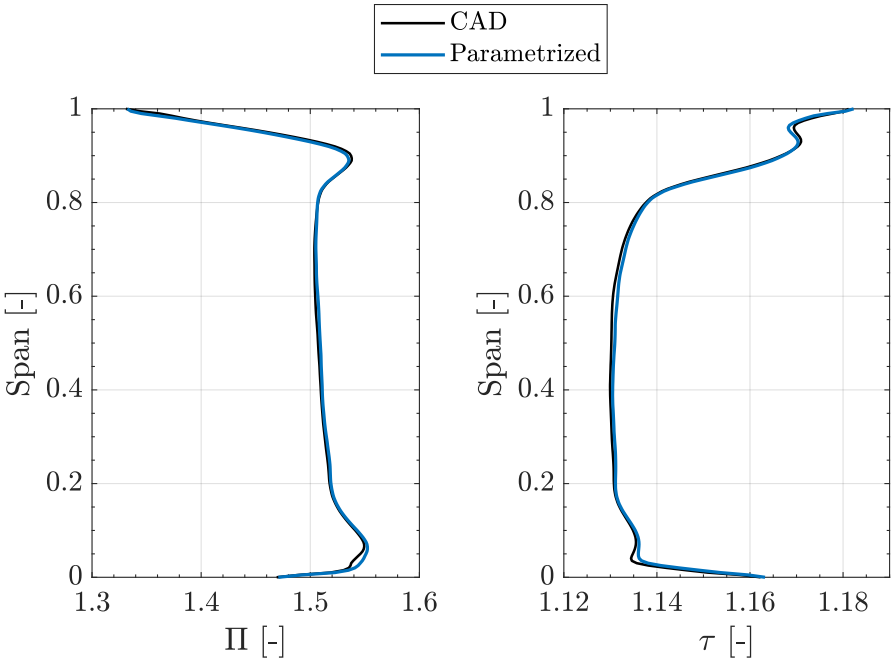

Figure 4.8: Comparison of the total pressure ratio (left) and total temperature ratio (right) radial profiles at the rotor outlet between CAD blade and parametrized blade.

Regarding the local quantities, Fig. 4.8 shows the total pressure and total temperature ratios compared in the stationary frame of reference at the rotor outlet. Here as well the quantities show variance that is considered negligible. The slight increase in total pressure at around 5% of the span height is possibly the biggest difference of the parametrized blade, possibly due to the absence of the previously-discussed recirculation zone near the trailing edge of the blade (the streamlines difference is not shown for brevity).

Finally, the blade loadings displayed in Fig. 4.9 at 50% and 95% of the span are both almost overlapping, except mainly for the area on the pressure side around 10% of axial chord for Fig. 4.9a.

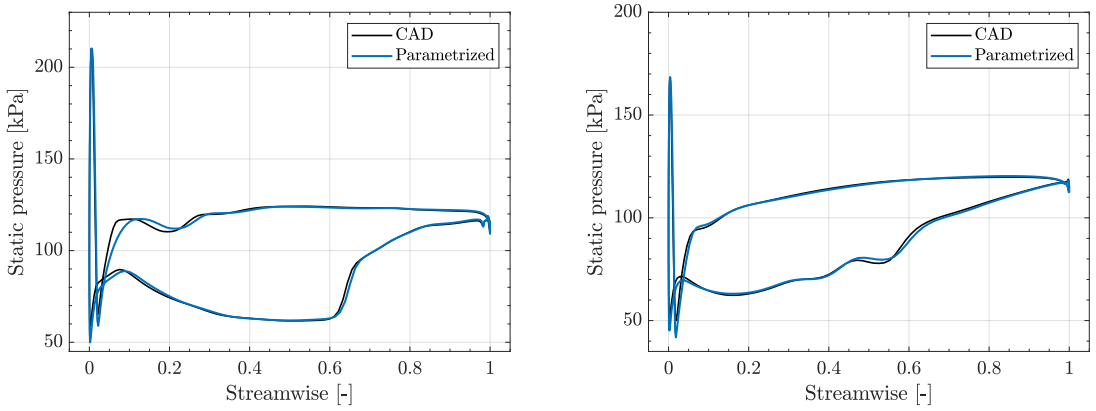

Figure 4.9: Blade loading at 95% (a) and 50% span height (b) compared between the CAD blade and the parametrized blade.

All in all the parametrization method, despite possible improvements in the geometry to better match the original CAD blade, seems to be accurate enough to describe the original flow when considering this operating point, with this grid. It can then be inferred that the change of flow characteristics between geometric variations and parametrized blade are valid to use to describe changes compared to the CAD blade as well.

4.3 Blade modifications

In this section, the main contribution of the study is presented where sets of blades, each with two blades modified in opposite directions, are described and the resulting flows compared to the standard parametrized blade. The parameters to be modified for each blade set, and their amount of change, are summarised in Tab. 4.1.
It was chosen to apply the modifications with the same amount of relative change on the whole blade, e.g. in blade set 4 the thickness of each layer is modified by 12%, resulting in a larger absolute thickness change in the thicker layers at the bottom compared to the ones at the top. By using relative changes, the variation is neither negligible nor unrealistically-large for any part of the blade.

4.3.1 Blade set 1—stagger angle

Beginning with the first blade set, the stagger angle has been modified by 1.6% in the positive and negative directions, equating to roughly 0.4 degrees of change. The global

Blade set	Parameter modified	Amount
1	ξ	$\pm 1.6\%$; $pos_\xi = 0.5$
2	$curl_{LE}$	$\pm 0.8\%$
3	$curl_{LE}$, $curl_{TE}$	$\pm 0.8\%$
4	t_{max}	$\pm 12\%$
5	t_{LE}	$\pm 12\%$
6	$tipgap$	$\pm 5\%$ (± 0.04mm)

Table 4.1: Modified blade parameters.

quantities in Fig. 4.10 show that an increase in stagger angle leads to a reduction in mass flow rate and total pressure ratio, while no significant change is seen in the isentropic efficiency. The former conclusions align with the fact that an increase in stagger angle will respectively increase the exit blade angle and, as it corresponds to a decrease in incidence angle, decrease blade loading overall.

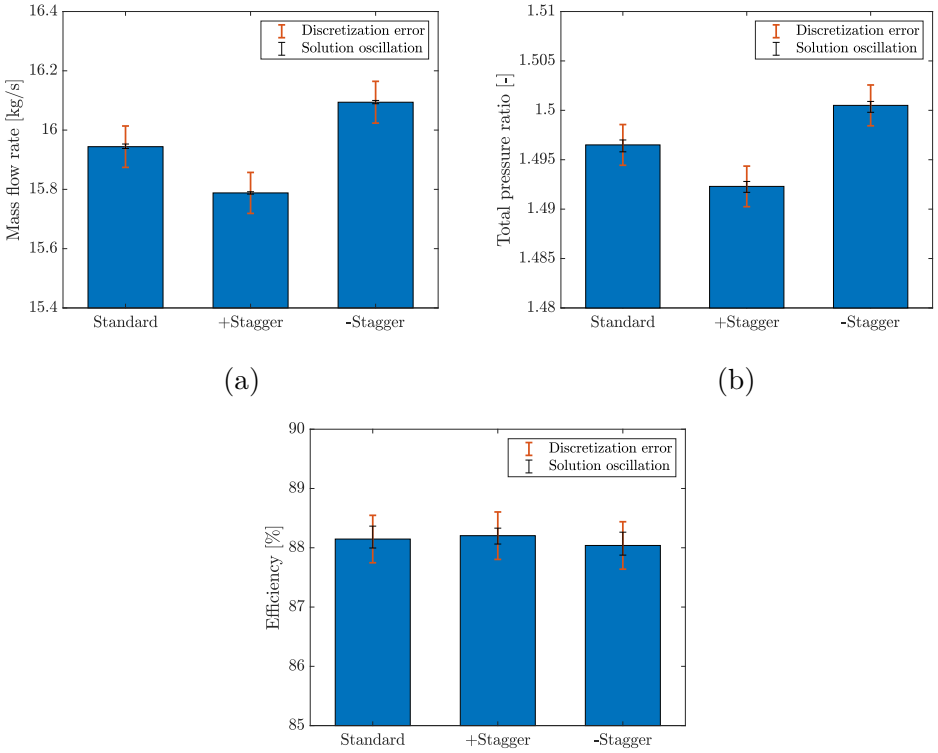

Figure 4.10: Comparison of mass flow rate (a), total pressure ratio (b), and isentropic efficiency (c) between the standard blade and the blades modified in stagger angle.

On the subject of blade loading, a slight reduction is indeed found when looking at the two span heights used for this study. In Fig. 4.11a the pressure side is affected close to the leading edge, indicating a faster flow when increasing the stagger angle due to

the decreased incidence. Not shown here, a blade-to-blade plot of the difference in Mach number between the positive and negative variations corroborates it, along with a slight change in the angle of the tip leakage vortex: the increase in stagger angle leads to this low velocity area being more parallel to the chord of the blade. Remarkably, there does not seem to be a change in the shock impingement position on the suction side. This might be due to a combination of choice in amount of change, geometry, and discretization error; however a slight variation in the shock's detachment from the leading edge is found, being more distant in the positive case.
Fig. 4.11b shows a similarly-small change in blade loading when considering the 50% span height.

Overall, this modification produced limited variations in the flow, despite significantly impacting global quantities.

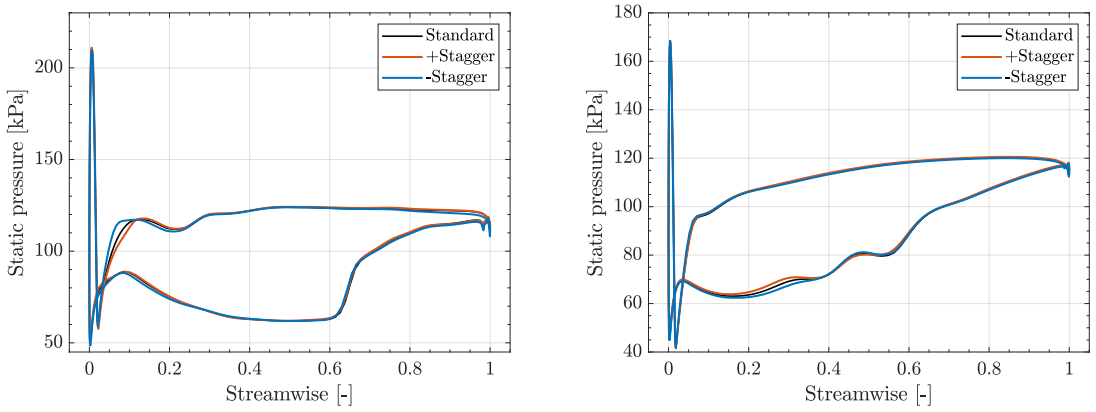

Figure 4.11: Blade loading at 95% (a) and 50% span height (b) compared between the standard blade and the blades modified in stagger angle.

4.3.2 Blade set 2—LE curl

The second blade set features the addition of a curl at the leading edge of 0.8% of the original θ_{LE} value in both directions. The global quantities in Fig. 4.12 are all impacted, with all being decreased especially in the positive change case (increase in leading edge metal angle β_{in}). It is clear that there is a high sensitivity to this parameter, as seen in the next quantities analysed.

Mach contours at 95% of the span height are compared between each other in Fig. 4.13, and show significant variance as well. To begin with, the positive change decreases

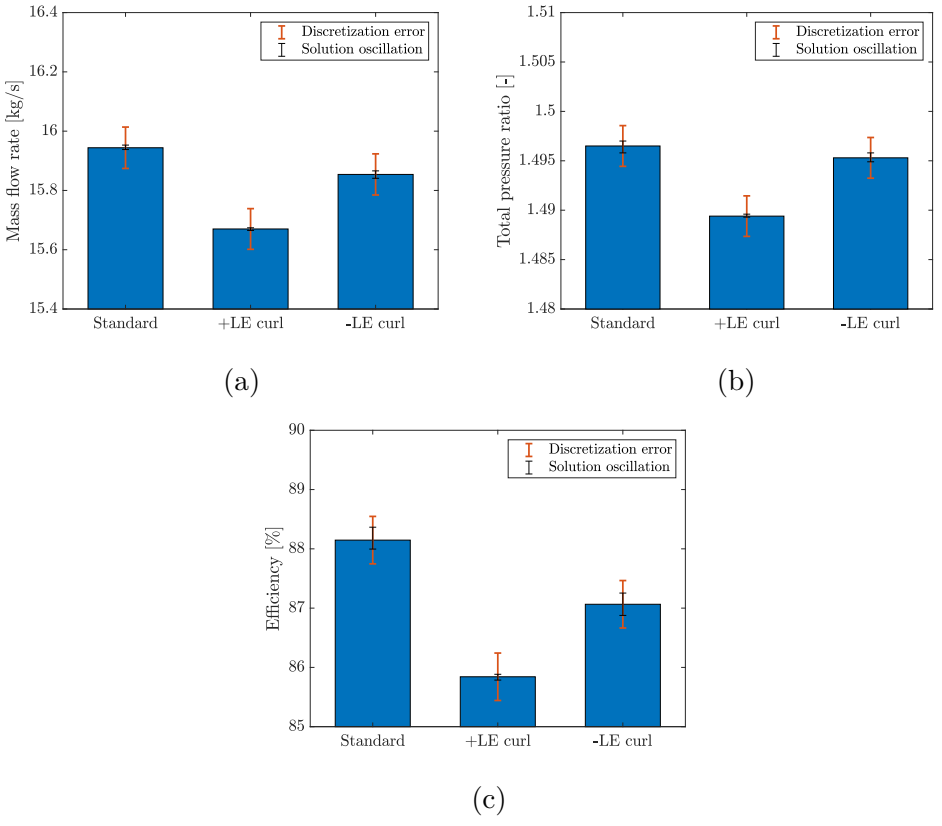

Figure 4.12: Comparison of mass flow rate (a), total pressure ratio (b), and isentropic efficiency (c) between the standard blade and the blades modified in leading edge curl.

the angle between original chord and bow shock, making it more acute and thus impinging on the neighbouring blade more downstream. This, as well as the stronger shock due to higher velocities in the passage, seems to hinder flow reattachment.
The tip vortex is also significantly strengthened, being possibly the main reason for the stark decrease in isentropic efficiency for this case, along with a non-ideal blade loading caused by the significant increase in flow velocity on the pressure side.

On the other hand, the negative change features opposite behaviour, with the widening bow shock moving the shock-induced separation upstream, aiding reattachment; the area with high velocity on the pressure side is also reduced to the point where it does not go over Mach 1, and finally the tip leakage vortex seems similar in strength, if not weaker. Despite these seemingly-positive changes, the upstream motion of the shock means a reduction in overall blade loading compared to the standard case due to the pressure increase being located on the suction side. Indeed, the total pressure ratio at the rotor outlet in Fig. 4.14 confirms this reduction is coming mainly from the sections where the shock is stronger, above 60% of the span height. The cause is however the conjunction of the aspect just explained with an increase in the height of the shock-induced separation

near the tip, shown later.

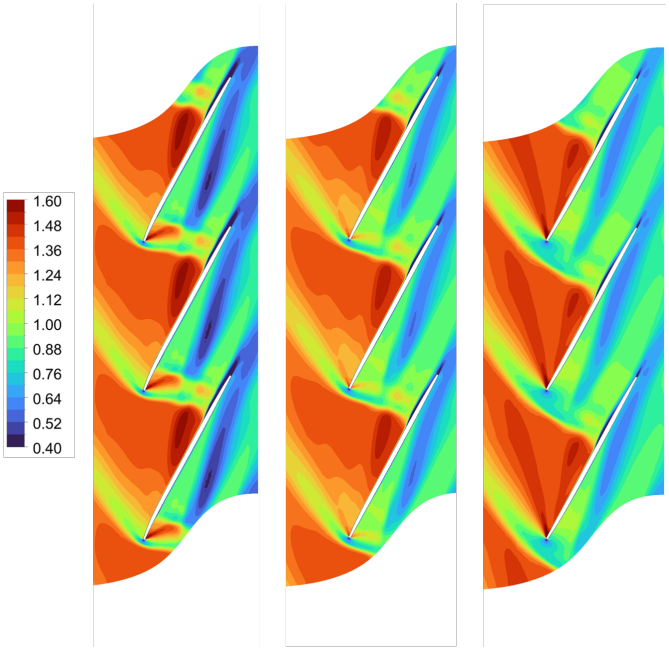

Figure 4.13: Blade-to-blade plot of the Mach number at 95% of the span of the increased LE curl (left), standard (centre), and decreased LE curl (right) blades.

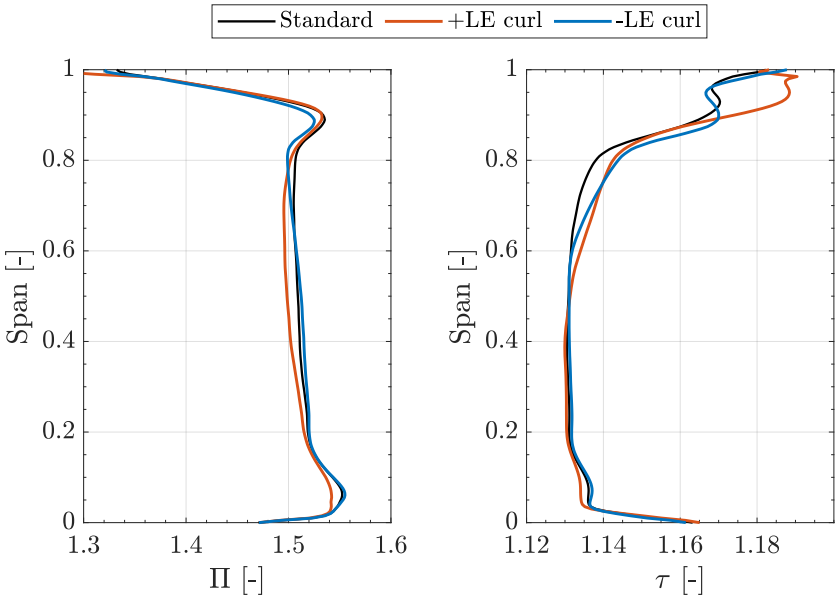

Figure 4.14: Comparison of the total pressure ratio (left) and total temperature ratio (right) radial profiles at the rotor outlet between the standard blade and the blades modified in leading edge curl.

4.3.3 Blade set 3—LE & TE curl

In addition to the leading edge curl, in this blade set a trailing edge curl is present of the same relative difference of ±0.8%. The changes are applied in the same sign, so that both θ_{LE} and θ_{TE} increase or decrease, meaning in extreme changes the blades will acquire a C shape with the concave side on the pressure or suction side respectively. The small θ_{TE} values result in the change applied here being lower than the one at the leading edge. Still, there is significant variation in results between this set and the previous one.

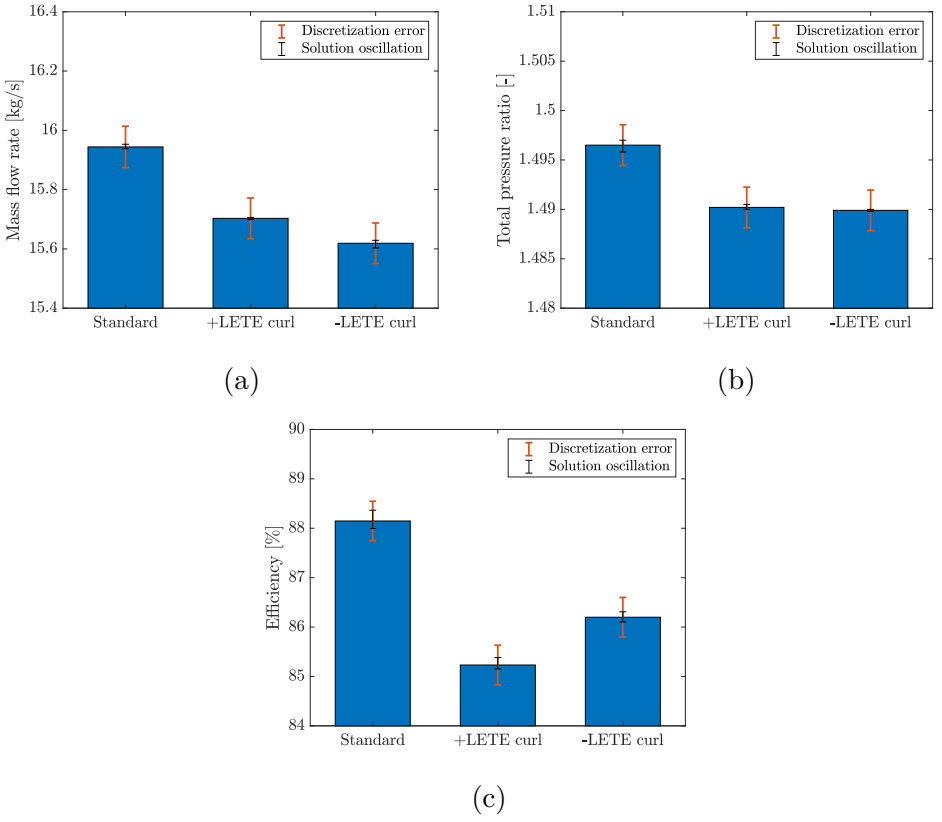

Figure 4.15: Comparison of mass flow rate (a), total pressure ratio (b), and isentropic efficiency (c) between the standard blade and the blades modified in leading and trailing edge curl.

The global quantities in Fig. 4.15 show that little is different between a positive addition of both leading and trailing edge curls and applying it positively only at the leading edge, except for the efficiency, which gets further decreased.
On the other hand, for the negative case now the mass flow rate and total pressure ratio are not between the standard case and the positive change, but are lower and equal to the positive case respectively. The effects at 95% of the span are not dissimilar to what is found in Fig. 4.13, but now feature a stronger tip vortex and a downstream (upstream) motion of the shock-induced separation for the positive (negative) case.

When considering blade loading, in Fig. 4.16, the first 50% of the axial chord presents almost no differences compared to the leading edge curl cases, while for the last half of the profiles a ”thickening” and ”thinning” of the blade loading, respectively for the positive and negative variation, is now present. The thinning, along with the further motion upstream of the shock, should be the underlying cause of the decrease in total pressure ratio for the negative case: the quantities at the rotor exit of Fig. 4.17 are almost the same for the positive cases, while the the negative case has stronger variations of the same kind found in the negative case of the leading edge curl change.

The remarkable differences are also found in the streamlines plots of Fig. 4.18, where the last two sets of blades are compared to the standard case and between each other. It can be seen that a positive change leads to the hub-corner separation line moving towards the tip, especially when a trailing edge curl is applied as well. The shock-induced separation is also visibly moving downstream as mentioned, while for the negative change it moves upstream and expands radially for both cases, but more so for the blade with trailing edge curl on top of the leading edge curl.

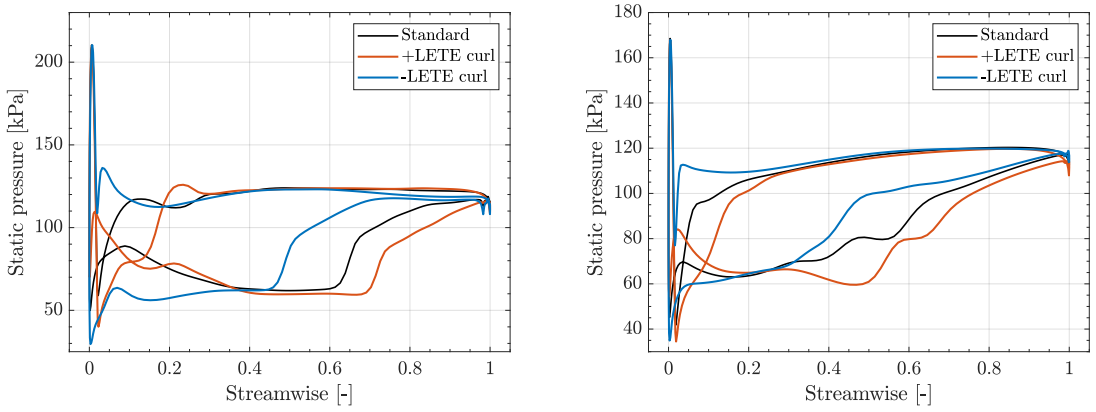

Figure 4.16: Blade loading at 95% (a) and 50% span height (b) compared between the standard blade and the blades modified in leading and trailing edge curl.

4.3.4 Blade set 4—maximum thickness

A change in the maximum thickness of each profile of 12% of the original value is applied in the two directions, thickening or thinning it respectively for the positive and negative change. Fig. 4.19 displays the global quantities of interest, where it is visible a downward trend for the mass flow rate and total pressure ratio if thickness is added, and the opposite happens with a reduction in thickness. The isentropic efficiency is not varied in a

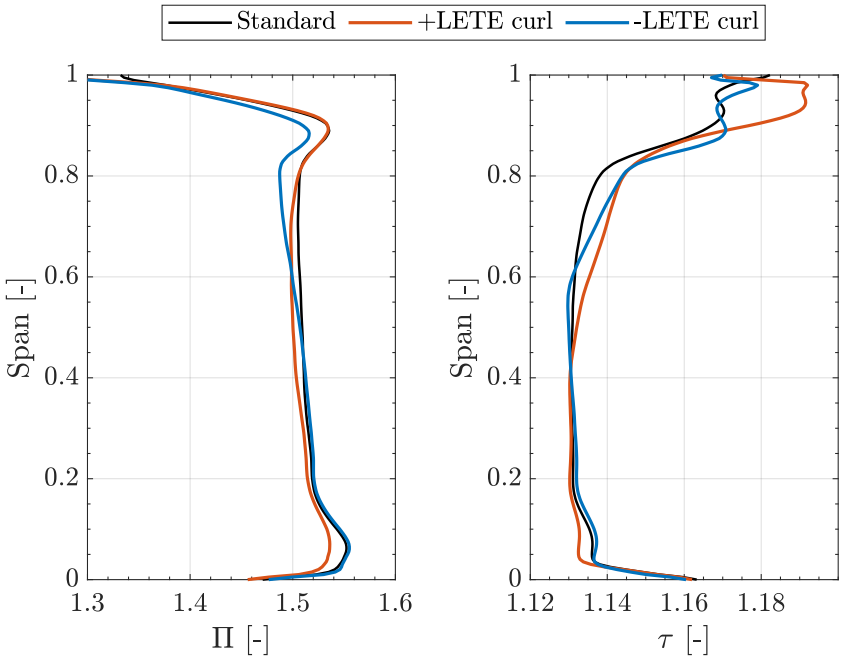

Figure 4.17: Comparison of the total pressure ratio (left) and total temperature ratio (right) radial profiles at the rotor outlet between the standard blade and the blades modified in leading edge and trailing edge curl.

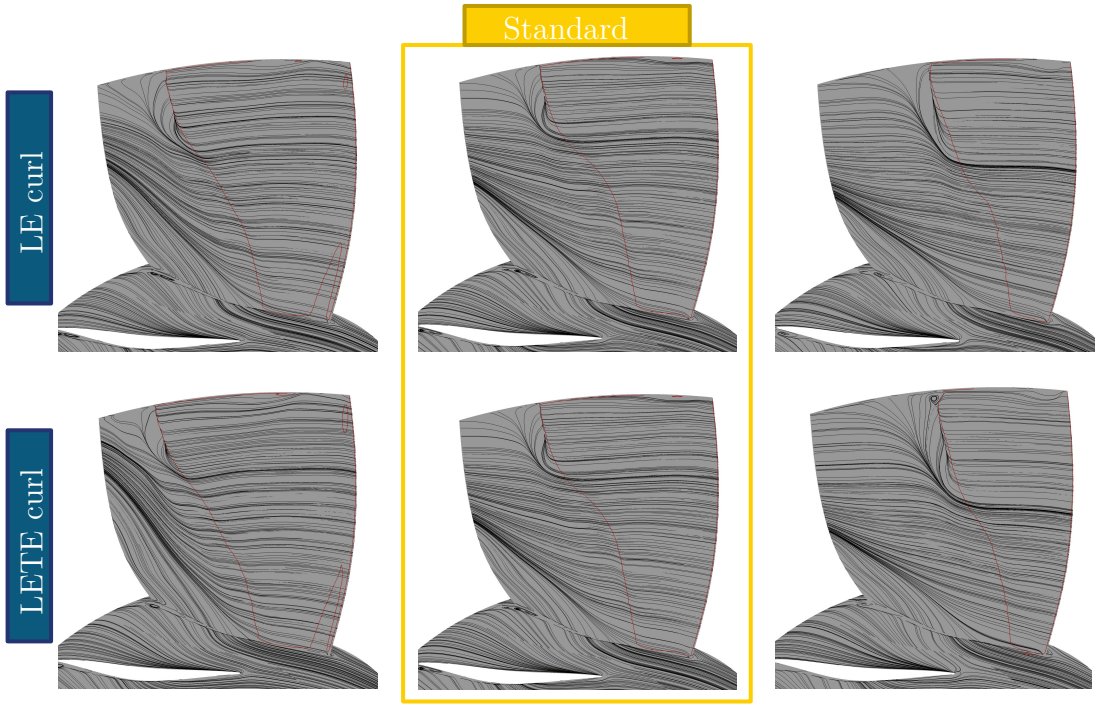

Figure 4.18: Comparison of the blade streamlines: the top row is for the blade set no.2 while the bottom row for blade set no.3. On the left the positive change, at the centre the standard case, on the right the negative change.

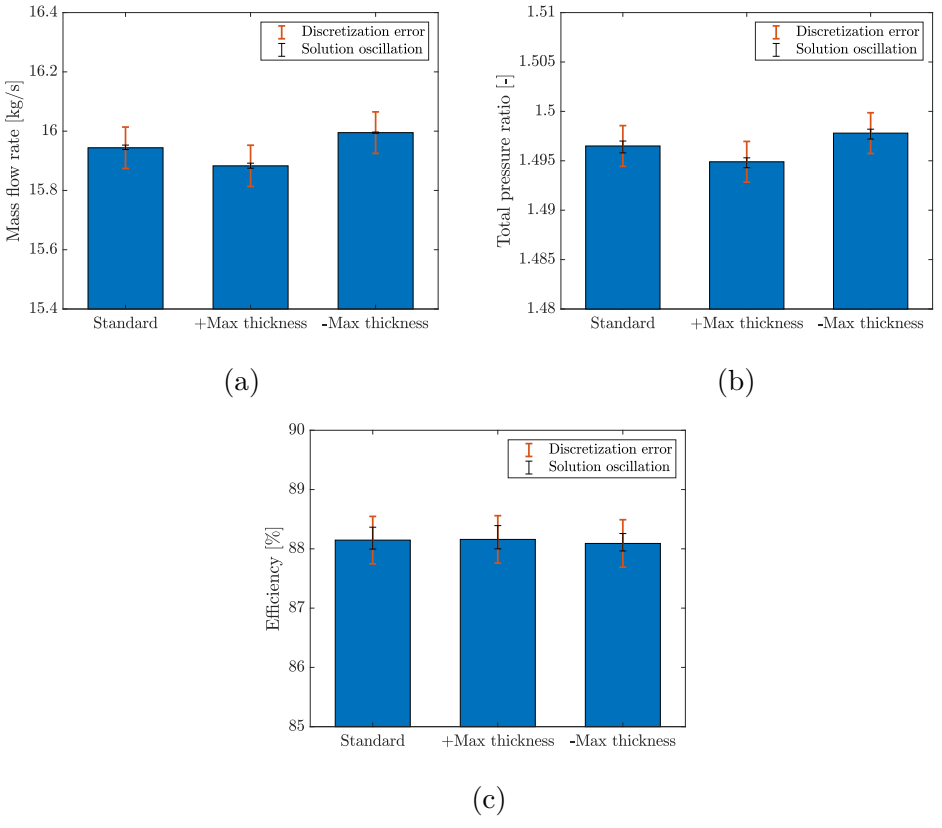

Figure 4.19: Comparison of mass flow rate (a), total pressure ratio (b), and isentropic efficiency (c) between the standard blade and the blades modified in maximum thickness.

significant way. The result for the total pressure ratio is in line with the study by Lange et al. [9], with a thickened profile causing higher total pressure losses due to a thicker wake, however the solution oscillation does not let us evaluate and compare the impact on the efficiency as well. The stronger wake should also be the main cause of the variation in mass flow rate, as no significant difference is found in tip vortex or other flow blockage phenomena, corroborated by the slight changes in total pressure and total temperature ratios at the rotor exit, in Fig. 4.20, only being present between 25% and 80% of the span height where hub, tip vortex, and shock-induced separation are not affecting the flow.

4.3.5 Blade set 5—LE thickness

Along with the maximum thickness change, another parameter that has been found in various studies to significantly vary the performance of compressors is the thickness of the leading edge. Again, a 12% variation from the original value of each layer of the blade is applied in the positive and negative directions (respectively thickening and thinning the blade's leading edge), with the results of the global quantities in Fig. 4.21 being in line

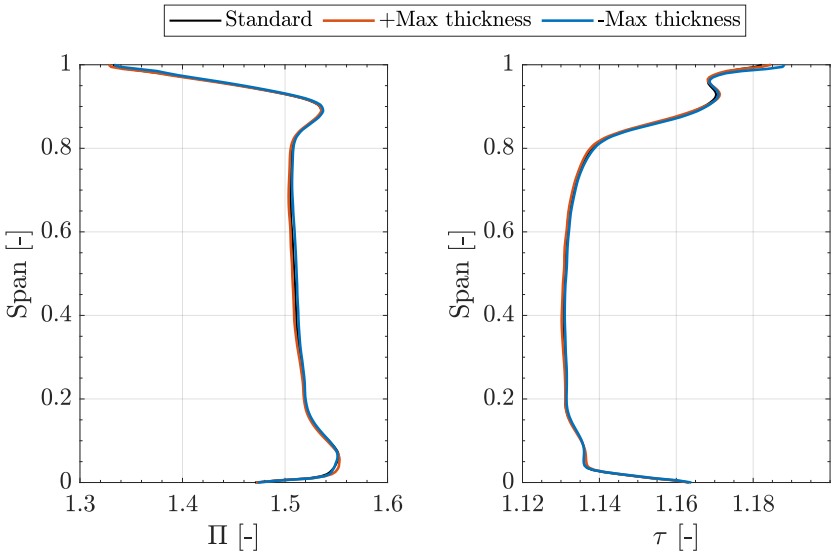

Figure 4.20: Comparison of the total pressure ratio (left) and total temperature ratio (right) radial profiles at the rotor outlet between the standard blade and the blades modified in maximum thickness.

with the maximum thickness change blade set and with the literature. In particular, the mass flow rate and total pressure ratio feature the same trends as with the last blade set, albeit with a lower intensity, however this time the efficiency is impacted in a significant way, with the thicker leading edge reducing it while the thinner one increasing it.

When looking at the blade loading curves in Fig. 4.22, it can be seen that the thickening of the leading edge causes not only a higher velocity of the flow just after the leading edge, but also the larger low-velocity area around the stagnation point means the bow shock is further detached from the blade and pushes upstream the shock impinging on the suction side, decreasing loading of the higher sections of the blade. Thickening the leading edge of the blade is found to reduce the efficiency (and vice versa for the thinning of it) mainly through the effects in the tip region, where the tip vortex increases in strength and the total temperature ratio goes up.

4.3.6 Blade set 6—tip gap

The final blade set features a variation of 5% in tip gap compared to the standard 0.8mm one, corresponding to the distance found near the peak efficiency operating point. This set was found not to impact the standard results in any meaningful way as confirmed by previous research on this configuration [21], except for a slight increase in mass flow rate when the gap is increased in size, and a decrease when the gap is made tighter.

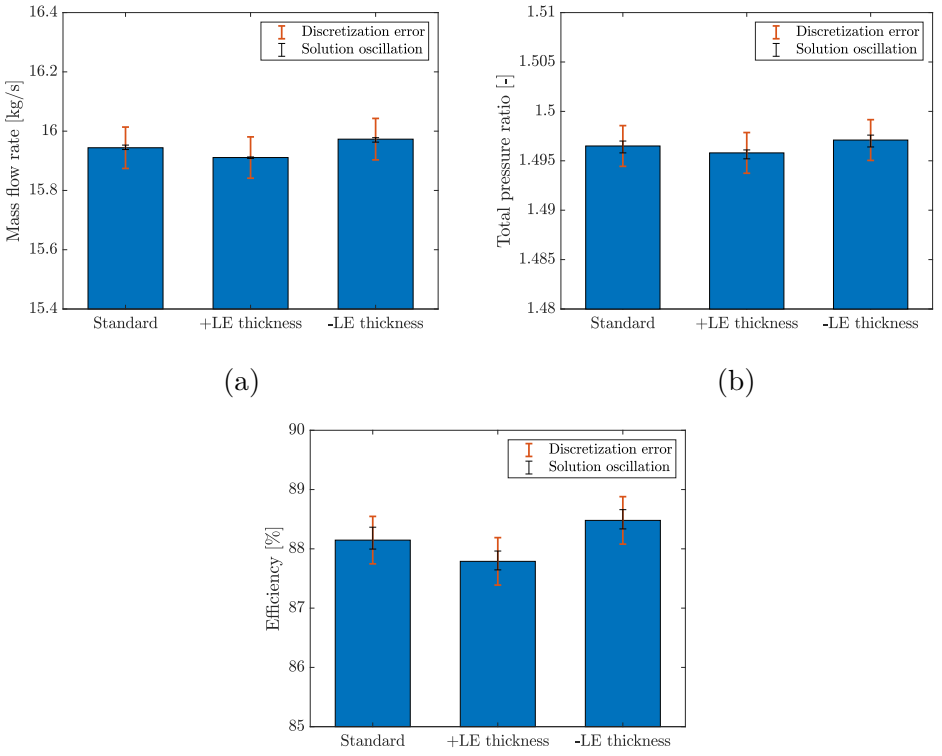

Figure 4.21: Comparison of mass flow rate (a), total pressure ratio (b), and isentropic efficiency (c) between the standard blade and the blades modified in leading edge thickness.

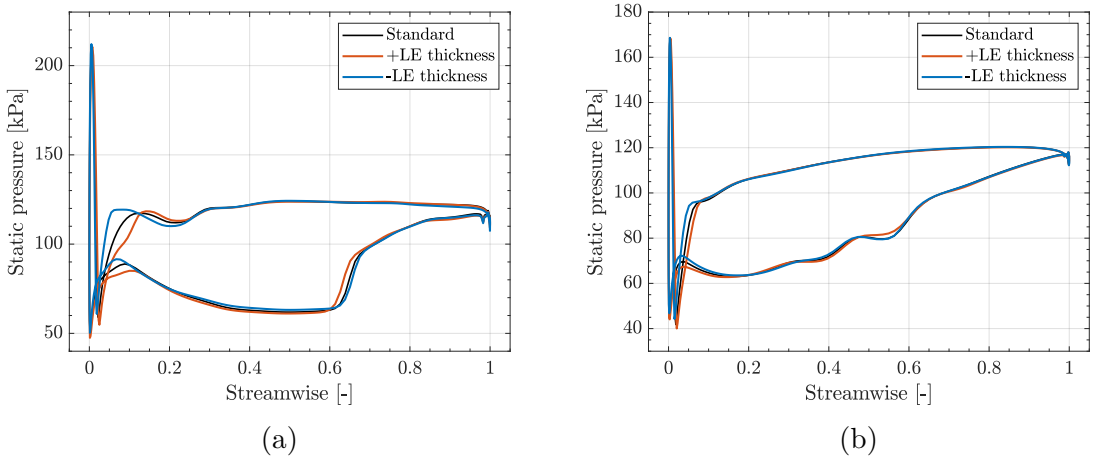

Figure 4.22: Blade loading at 95% (a) and 50% span height (b) compared between the standard blade and the blades modified in leading edge thickness.

4.4 Full annulus

The final simulation was performed on the full annulus configuration, with a single mis-staggered blade. The stagger angle of this blade was increased by 2% compared to the 1.6% of blade set no.1 to increase the possible effects on the flow.
As expected, the global quantities are found to lie between the standard case and the ones of blade set no.1, as shown in Fig. 4.23, except for the efficiency which does not feature a significant change.

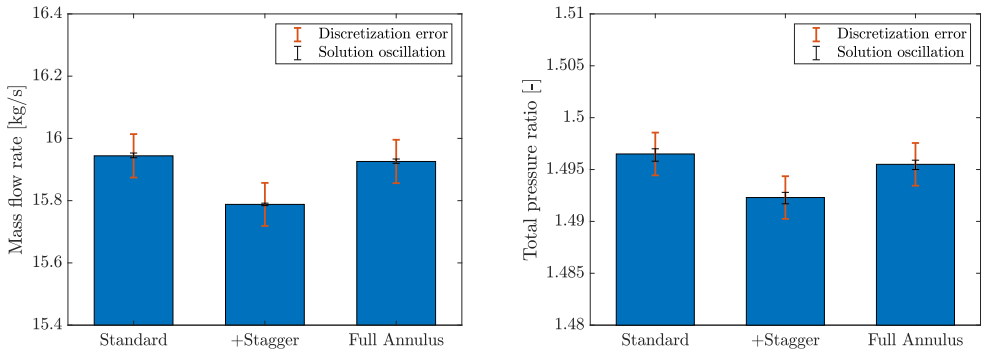

(a) (b)

Figure 4.23: Comparison of mass flow rate (a) and total pressure ratio (b) between the standard blade, the mistaggered blades of blade set no.1, and the full annulus with the single mistaggered blade.

Regarding the local quantities, the blade loading at 95% of the span of Fig. 4.24 is plotted for all the blades, where it can be seen that the misstaggered blade features the same kind of profile in the leading edge area as found in blade set no.1 previously, while at the midchord higher pressure is recorded on the pressure side which was not found before, finally with lower pressures in the trailing edge areas. These variations from the standard case could be due to the different neighbouring passages and/or the higher amount of geometric variation applied in this case.
The other important change is the position of the shock which was not found in blade set no.1, however this, while it is at least in part an effect of the geometry, will be later shown it could be due to other factors.

Most of the other blades stay identical to the standard case (of the single passage simulations) and close to each other, resulting in darker black points, however the shock impinging on the suction side is now moved upstream. Two of the blades however feature pressure profiles closer to that of the misstaggered blade in the leading edge area, with one showcasing a lower pressure than all the others on the pressure side. These two blades

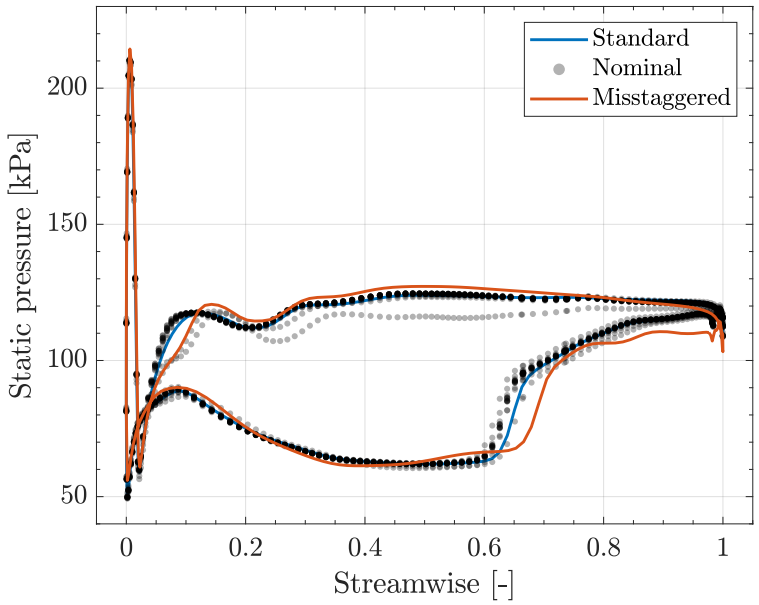

Figure 4.24: The blade loading profiles on the rotor blades at 95% of the span height vs normalised axial chord.

also feature a motion of the shock impingement upstream and downstream of the others. In particular: the blade preceding the modified one has the shock slightly upstream, while the blade following it is the one with a more downstream shock and the lower pressure on the pressure side.

The misstaggered blade has a shock geometry that is slightly different from the others, given from the stagnation point moving towards the suction side of the blade, in a way rotating the bow shock while also detaching it slightly more. This seems to be the cause of the impingement going more upstream on the preceding blade. On the other hand, the change in stagger angle modifies the passage's geometry between the misstaggered blade and the one following, with the tightening of the passage leading to higher velocities, and as such lower pressures. All these findings are shown in Fig. 4.25 where the 95% span Mach profiles are compared with the standard case single-passage simulation, albeit the limitations of this set up start to show here: it is quite difficult to notice the variations as CFD-Post was unable to create difference plots outside the single passage domain. It was also impossible to create blade-to-blade plots of the full annulus solution due to various problems within the Turbo components not correctly visualising the domains. As a result, the plot is only a view of the machine from directly above the modified passage, distorting the shapes away from it.

In Fig. 4.25, here we can also see the aforementioned possible main cause of the

shock impingement moving downstream on the mistaggered blade: a sharp line creates unmatching velocity profiles, and this is found to be exactly at the interface between the "negative gap" subdomain and the modified rotor one. Unfortunately these phenomena are possible when an interface is present, and especially so when the interface is between meshes with different elements such as here, where one side is made only of hexahedra while the other has a mix of tetrahedra and prisms. That said, in the pressure field this mismatch is not as severe. Finally, the tip vortex varies in all the shown passages.

The main takeaway is that the change in stagger angle in a single blade created modifications in the loading of the neighbouring blades: this could very well be the starting point for the alternate passage divergence phenomenon described in Lu et al. [12], of course not captured in this study due to the absence of coupling between fluid and the BLISK's structure.

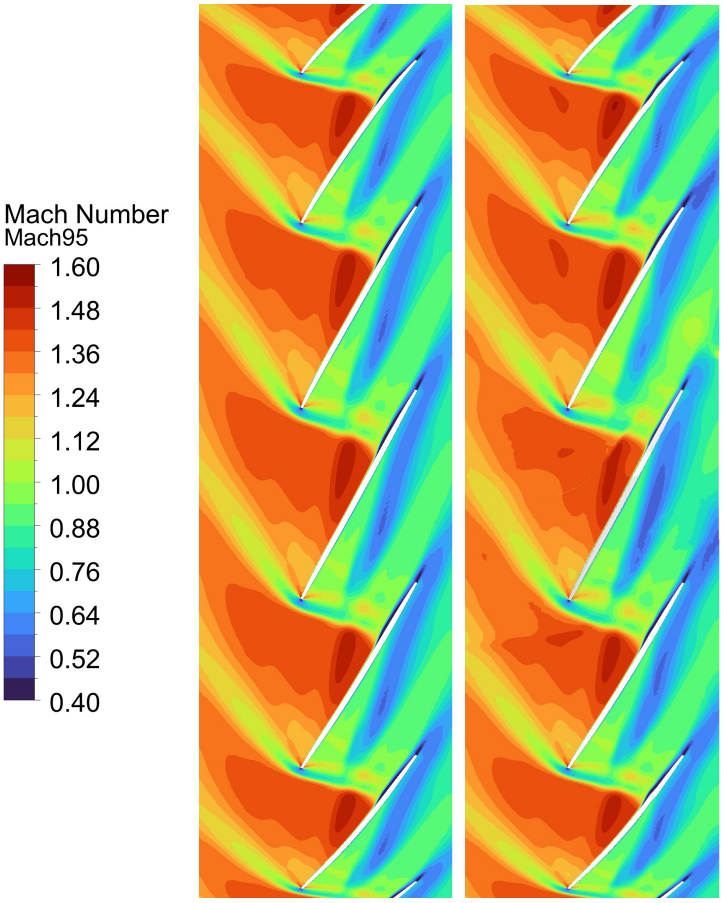

Figure 4.25: Comparison of Mach number at 95% of the span height between standard case (left) and full annulus with a single modified blade (right, with the modified blade in the centre, slightly greyed).

Other quantities to look at would be the rotor exit ones. This time, these are shown circumferentially to showcase any passage-to-passage variation that may appear. When

in the relative frame of reference, the total pressure profiles in Fig. 4.26 are shown to vary outside the passages neighbouring the modified blade, especially the three passages following it (negative angles). When moving downwards to the 2% span, it is interesting to note that some kind of pattern emerges, with the points of minimum in the blades following the misstaggered one having a stronger pattern that gets dampened when reaching the passage opposite to the modified one.

These patterns are found with other quantities as well, such as with pressure or Mach number, but only at span heights close to the shroud or close to the hub. An example of this is in Fig. 4.27, where at 98% of the span it can be seen a one-every-four pattern in the pressure peaks.

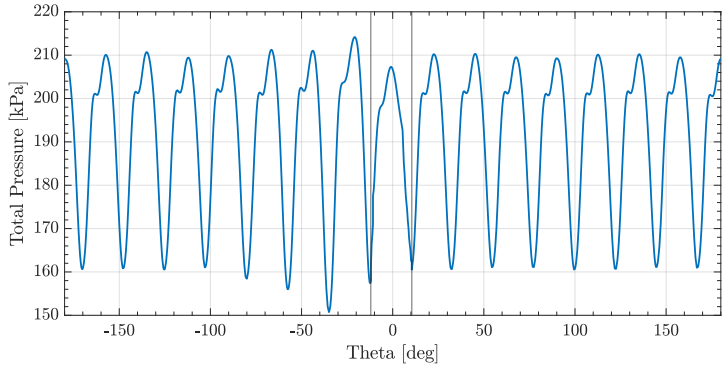

(a)

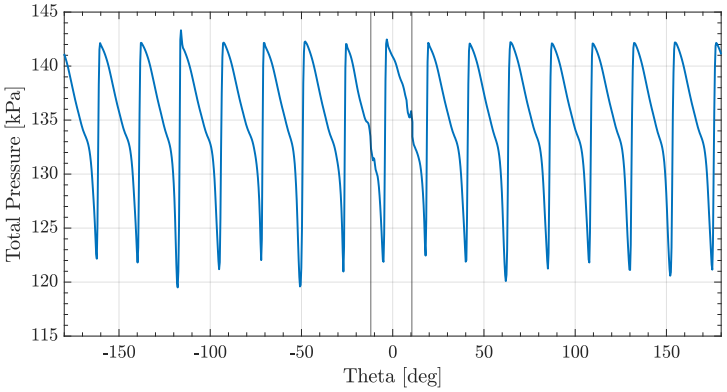

(b)

Figure 4.26: Circumferential profile at rotor exit at 95% (a) and 2% (b) of the span height of the total pressure in the relative frame of reference.

One problem that was found in the solution is that only in the rotor exit part of the gap domain following the modified blade, there is a high velocity area close to the shroud that is possibly non-physical, with for example the total pressure ratio in the stationary frame of reference going under 1.0, a glimpse of this can be seen when approaching the 0 degree angle in Fig. 4.27. Since it only happens within the gap subdomains, it could

be a result of the presence of multiple interfaces close together, one of which being a mixing plane, and with different kinds of meshes—discrepancies between the domains at the interfaces can be seen also in Fig. 4.26b.

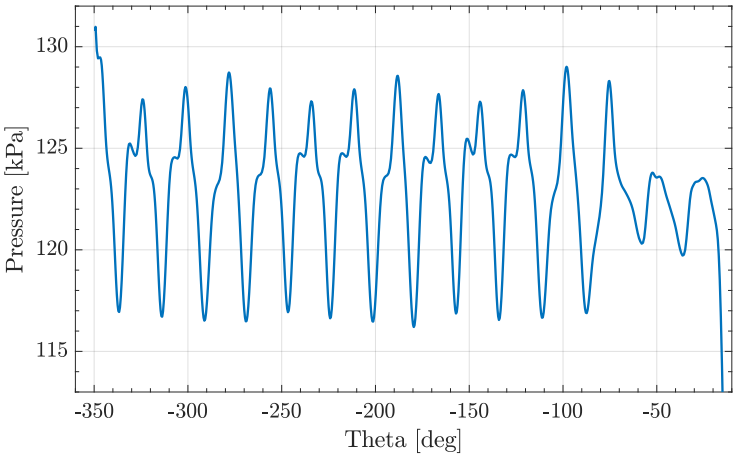

Figure 4.27: Circumferential profile at rotor exit at 98% of the span height of the pressure only for the nominal blades.

Chapter 5

Conclusions and future work

The present work presented a study on the impact of different kinds of geometric uncertainties in turbomachinery blades on the flow inside the front stage of a high pressure transonic axial compressor through the use of CFD. The aim is not only to investigate the variations, but also to develop the tools and processes necessary for future studies in the institute regarding geometric uncertainties, in the form of scripts to modify blades, single passage CFX setups and a full-annulus CFX setup with a single differing rotor blade.

First, a reference single passage setup of the TUDa-GLR-OpenStage geometry was created and a mesh independence study conducted on it to find a grid that could appropriately portray the flow in the machine, and also to estimate the discretization error on the quantities of interest. The final result of this was found to be in accordance with previous studies of the same configuration, and was used to create a speedline at the design speed of the compressor.
The initial geometry of the rotor blade was then parametrized in order to easily modify it as needed to reproduce the researched uncertainties. This new geometry is then tested against the original to assess the quality of the blade's reproduction: it was found that the surfaces themselves presented non-negligible differences compared to the original one, however these did not impact the flow in any significant way.

Matlab scripts are then created in order to provide an easy-to-use tool that can systematically modify a given parametrized blade by adding the most common kinds of geometric uncertainties found in turbomachinery: circumferential and axial positions of leading and trailing edges, curl of leading and trailing edges, thickness of leading and trailing edges, maximum thickness, blade stagger angle, tip gap (this last one being actually handled

from within Ansys).

Six sets of blades are created, each showcasing a different parameter variation in the positive and negative direction. At the chosen level of change, the tip gap was found not to impact the flow in any significant way, while the maximum thickness only affected the machine in the global quantities, registering a reduction in mass flow rate and total pressure ratio as thickness is added, and vice versa for the removal of thickness. The stagger angle was found to affect the global quantities more, with the increase (reduction in incidence angle) reducing both mass flow rate and total pressure ratio, as well as slightly impacting the blade loading. The variations are found to be opposite when reducing the stagger angle.
Leading edge thickness change provided some variation in all the global quantities of interest, with the thickening reducing mass flow rate, total pressure ratio, and efficiency (with mainly the tip region phenomena impacting the latter); the opposite happens when thinning the leading edge. Blade loading was found to vary in the first 10% of axial chord especially at higher span heights, while also featuring a motion of the shock impingement on the suction side due to the variation in size of the low velocity area around the stagnation point.
Curl of the leading edge and of both leading and trailing edges by far are the factors that most impact the flow. All reduce the mass flow rate, total pressure ratio, and isentropic efficiency; especially the positive change in leading edge curl, and the negative change in trailing edge curl. These parameters were found to reduce the efficiency up to 3%. The addition of leading edge curl and of both leading edge and trailing edge curl cause a downstream shift in shock impingement, as well as an extension of the hub corner vortex (especially for the case with the trailing edge curl as well); the addition of leading edge curl causes a ”reversal” of the pressure and suction side near the leading edge, as well as a stronger tip leakage vortex, while the addition of curl at the trailing edge decreases pressure in the suction side towards the trailing edge. The decrease in leading edge curl was found to cause an upstream shift and a radial extension of the shock-induced flow detachment and an increase in blade loading in the first part of the profiles, while the decrease in trailing edge curl caused a reduction in loading towards the trailing edge.

A full-annulus simulation was then performed with a single blade featuring a higher stagger angle than nominal, slightly higher than the one in the single-passage simulations. It was found that the global quantities sit between the reference results and the ones where stagger angle is added to all the blades; blade loading is varied mainly in the misstaggered blade, now featuring a downstream shift in shock impingement, while the two surrounding

blades vary significantly in loading. All the blades except one also present an upstream motion of the shock impingement compared to the reference case, with the blade preceding the modified one having it move upstream compared to the nominal ones due to the further detachment of the bow shock from the misstaggered blade. Finally, variations in rotor exit quantities were found to extend beyond the passages neighbouring the modified one, with some also featuring some kind of pattern in the tip and hub regions.

All in all, while the findings are satisfactory, it is realized that this kind of set up for a full-annulus simulation might present inaccuracies: the choice of keeping the workflow similar to what was previously done meant the creation of new domains without the use of TurboGrid, leading to interfaces close between each other with differing kinds of elements, one of which being a mixing plane. Such configuration led to discrepancies in flow quantities and a high velocity area on the rotor outlet interface that does not seem realistic. It would be beneficial to switch to defining the fluid domain through a negative volume, removing the need for interfaces within the rotor subdomain as well as the need for manual creation of the gap domains for every blade modification. Once this kind of study is conducted, the impact on the flow of an unsteady simulation could be investigated due to the unsteady nature of it, and it would be especially worthwhile to include partial or full flow-structure coupling if investigating phenomena such as APD.

On the subject of the single passage simulations, further research could be directed towards the creation of a grid that is able to capture the differences between the CAD blade and the parametrized one: this is done as the changes seen in Section 4.2 might be in the order of magnitude of the actual geometric variance found in the R1 rotor blades, and therefore inquiring into the flow variations of the actual geometric differences would necessitate a grid accurate enough to do it.
The tools developed in the course of this thesis can be used in future studies not only to further investigate geometric uncertainty effects through the use of Monte Carlo simulations for example, but also to conduct performance optimization or to more closely match the shape either of the CAD blade and/or of the real scanned blades, or to simulate the different kinds of geometry variations found in the blades.

Bibliography

[1] Goodhand, M. N., Miller, R. J., and Lung, H. W. (2012, June). The sensitivity of 2D compressor incidence range to in-service geometric variation. *Proceedings of the ASME Turbo Expo 2012: Turbine Technical Conference and Exposition, 8*, 159-170. doi:10.1115/GT2012-68633

[2] Klausmann, F., Franke, D., and Schiffer, H. P. (2022). Transonic Compressor Darmstadt Open Test Case–Unsteady Aerodynamics and Stall Inception. *Proceedings of Global Power & Propulsion Society.* doi:10.33737/gpps22-tc-71

[3] Bammert, K., and Sandstede, H. (1976). Influences of manufacturing tolerances and surface roughness of blades on the performance of turbines. *Journal of Engineering for Power, 98*(1), 29-36. doi:10.1115/1.3446107

[4] Balan, C., and Tabakoff, W. (1984, June). Axial flow compressor performance deterioration. *20th Joint Propulsion Conference* (p. 1208). doi:/10.2514/6.1984-1208

[5] Roberts, W. B. (1984, June). Axial Compressor Performance Restoration by Blade Profile Control. *Proceedings of the ASME 1984 International Gas Turbine Conference and Exhibit, 1.* doi:10.1115/84-GT-232

[6] Roberts, W. B., Prahst, P. S., Thorp, S., and Strazisar, A. J. (2005, January). The effect of ultrapolish on a transonic axial rotor. *Proceedings of the ASME Turbo Expo 2005: Power for Land, Sea, and Air, 6*, 381-387. doi:10.1115/GT2005-69132

[7] Garzon, V. E., and Darmofal, D. L. (2003). Impact of Geometric Variability on Axial Compressor Performance. *Proceedings of the ASME Turbo Expo 2003, collocated with the 2003 International Joint Power Generation Conference, 6*, 1199-1213. doi:10.1115/GT2003-38130

[8] Lange, A., Vogeler, K., Guemmer, V., Schrapp, H., and Clemen, C. (2009). Introduction of a parameter based compressor blade model for considering measured geometry

uncertainties in numerical simulation. *Proceedings of the ASME Turbo Expo 2009: Power for Land, Sea, and Air, 6*, 1113-1123. doi:10.1115/GT2009-59937

[9] Lange, A., Voigt, M., Vogeler, K., Schrapp, H., Johann, E., and Gu¨ mmer, V. (2010, October). Probabilistic CFD simulation of a high-pressure compressor stage taking manufacturing variability into account. *Proceedings of the ASME Turbo Expo 2010: Power for Land, Sea, and Air, 6*, 617-628. doi:10.1115/GT2010-22484

[10] Li, Y. L., and Sayama, A. I. (2014). Computational fluid dynamics simulations of blade damage effect on the performance of a transonic axial compressor near stall. *Journal of Mechanical Engineering Science, 229*(12), 2242–2260). 10.1177/0954406214553828

[11] Venkatesh, S., Suzuki, K., Vahdati, M., Salles, L., and Rendu, Q. (2020, September). Effect of Geometric Uncertainty on a One Stage Transonic Compressor of an Industrial Gas Turbine. *Proceedings of the ASME Turbo Expo 2020: Turbomachinery Technical Conference and Exposition, 2*. doi:10.1115/GT2020-16315

[12] Lu, Y., Lad, B., Green, J., Stapelfeldt, S., and Vahdati, M. (2019). Effect of geometry variability on transonic fan blade untwist. *International Journal of Turbomachinery, Propulsion and Power, 4*(3), 24. doi:10.3390/ijtpp4030024

[13] Suriyanarayanan, V., Rendu, Q., Vahdati, M., and Salles, L. (2022). Effect of manufacturing tolerance in flow past a compressor blade. *Journal of Turbomachinery, 144*(4): 041005. doi:10.1115/1.4052600

[14] Klausmann, F., Franke, D., Foret, J., and Schiffer, H. P. (2021). Transonic Compressor Darmstadt—Open Test Case. *Proceedings of Global Power & Propulsion Society.* GPPS-21-TC-0029. doi:10.33737/gpps21-tc-29

[15] Bakhtiari, F., Wartzek, F., Leichtfuß, S., Schiffer, H. P., Goinis, G., and Nicke, E. (2015). Design and Optimization of a New Stator for the Transonic Compressor Rig at TU Darmstadt. *Deutscher Luft- und Raumfahrtkongress 2015.*

[16] Menter, F. R., Kuntz, M., and Langtry, R. (2003). Ten years of industrial experience with the SST turbulence model. *Turbulence, heat and mass transfer, 4*(1), 625-632.

[17] ANSYS (2023). *Ansys CFX—Solver Theory Guide, Release 23.1.*

[18] ANSYS (2023). *Ansys CFX-Pre User's Guide, Release 23.1.*

[19] Roache, P. J. (1998). *Verification and validation in computational science and engineering*. Albuquerque, NM: Hermosa.

[20] Hansen, T., Munktell, E., Scheuerer, G., and Zwiener, K. (2022). Single-Stage Axial Transonic Compressor Flow–CFD Simulations Including a Systematic Quality Assurance Procedure. *Proceedings of Global Power & Propulsion Society*. GPPS-TC-2022-0012. doi:10.33737/gpps22-tc-12

[21] He, X., Zhu, M., Xia, K., Fabian, K. S., Teng, J., Vahdati, M. (2023). Validation and verification of RANS solvers for TUDa-GLR-OpenStage transonic axial compressor. *Journal of the Global Power and Propulsion Society, 7*, 13-29. doi:10.33737/jgpps/158034

[22] Siddappaji, K. (2012). Parametric 3d blade geometry modeling tool for turbomachinery systems. Master's thesis, University of Cincinnati.

[23] Nemnem, A., Turner, M., Siddappaji, K., and Galbraith, M. (2014). A Smooth Curvature-Defined Meanline Section Option for a General Turbomachinery Geometry Generator. *Proceedings of the ASME Turbo Expo 2014: Turbine Technical Conference and Exposition, 2*. doi:10.1115/GT2014-26363.

Acknowledgements

I would like to express all my gratitude to the people that have been around me in this journey, who in some way contributed to this achievement.

To the people most closely related to this path, my fellow THRUSTers: Pablo, Luis, Elvira, Paco, Cristian, Irene, and Belen. These are the people that were with me day-to-day, we all came together to knock down any sort of obstacle in this Master's degree, and also to party and have fun. The bond that formed is strong, and I love each of you for who you are, your knowledge, and your resilience. Hoping to have the honour to encounter at least some of you again in my life.

To the professors and researchers that have challenged, supported, and taught me what I now know, the people of great experience that guided me in these two years. You are the backbone of this experience and the creators of the current and future generations of engineers. I want to especially thank Nenad Glodic for his dedication to the THRUST program and the vibe he and the people at KTH created, Pietro Paolo Ciottoli for the great summer internship experience (as well as the Bachelor's thesis and his courses), Fabian Klausmann, Nicklas Kilian, and all the others at TUDa who welcomed me as a peer and showed me a stimulating working environment, and finally Koen Hillewaert for supporting me in this final work with his massive knowledge (the amount of which is almost frightening).

To my parents, who supported me in this experience from the get-go without questions, and my sister for inspiring me to look for new possibilities for my education.

To my dearest Pocci: Stefania, Christian, Sabrina, and Matteo. With them I shared years and years of goofiness, spent making each other laugh to the point of crying. These people are nothing short of family to me, and the amount of joy they release when we are together is astonishing. They have always been there in the ups and downs of life and I thank them for that.

Last, but not at all least, to my adorable partner in crime, my boo: to Stefania. She is the real backbone of this effort, the one that has been on my side cheering me on, always sharing a sweet word to make me smile even at the worst times, the person I most look forward to see every day, be it at home or thousands of kilometers away. Despite the distance I always felt you beside me, with the sweet feeling of being constantly infused in your light. This achievement is also yours, for you have always been the source of my inspiration, the person making me desire to push my boundaries to see if something better is possible.
Also the best person to watch movies with while in two different countries and complaining about the terrible buffering we are experiencing. Bloc.